Science Advances
AAAS

advances.sciencemag.org/cgi/content/full/6/23/eaay3998/DC1

Supplementary Materials for

Ultrathin water-stable metal-organic framework membranes for ion separation

Meipeng Jian, Ruosang Qiu, Yun Xia, Jun Lu, Yu Chen, Qinfen Gu*, Ruiping Liu,
Chengzhi Hu, Jiuhui Qu, Huanting Wang, Xiwang Zhang*

*Corresponding author. Email: xiwang.zhang@monash.edu (X.Z.); qinfeng@ansto.gov.au (Q.G.)

Published 5 June 2020, *Sci. Adv.* **6**, eaay3998 (2020)
DOI: 10.1126/sciadv.aay3998

This PDF file includes:

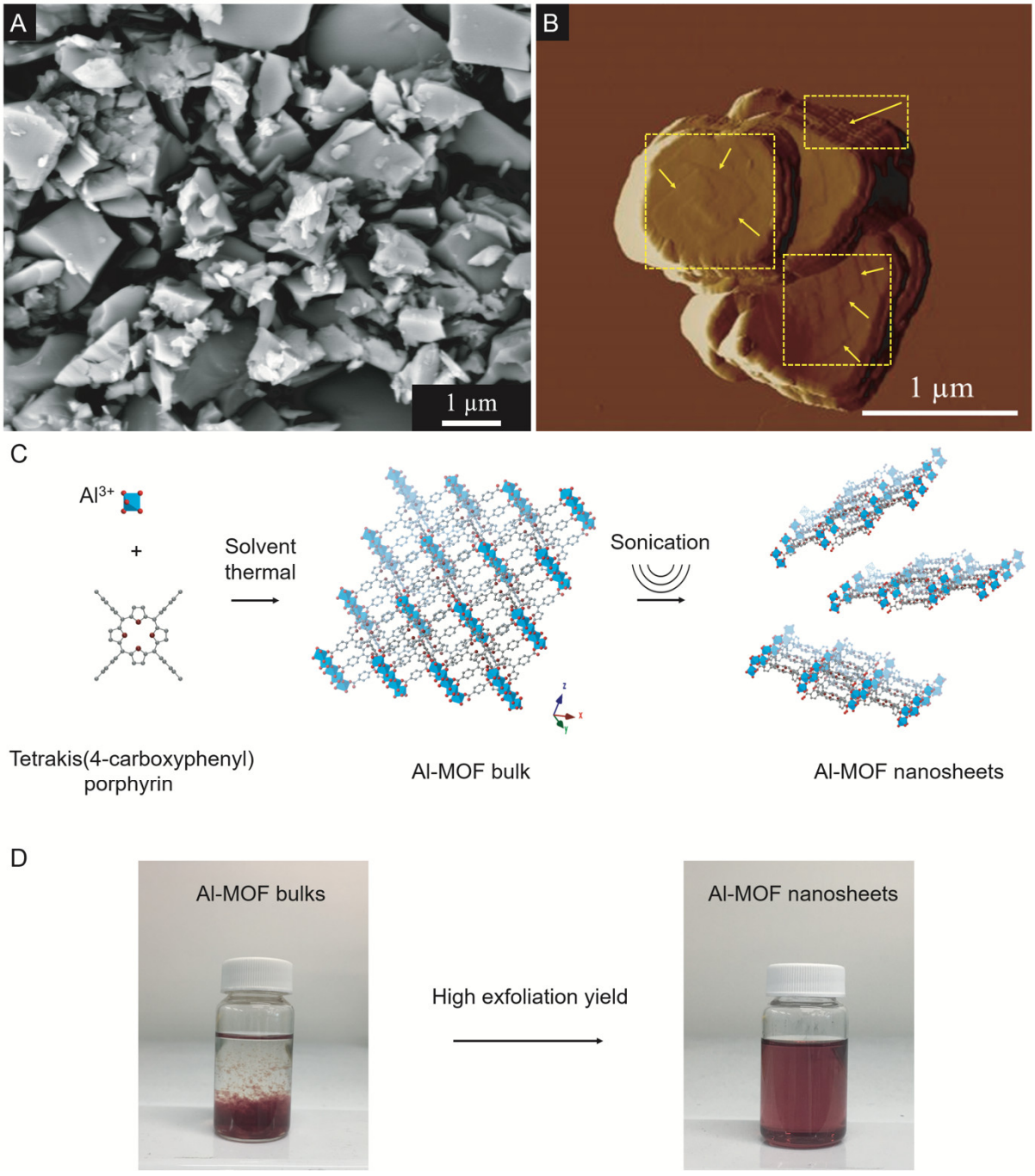

Fig. S1. Synthesis of Al-MOF nanosheets. (**A**) SEM image of Al-MOF bulks and (**B**) Representative AFM image of Al-MOF bulks. (**C**) Schematic illustration of the exfoliation process. (**D**) Photographs of Al-MOF suspensions in ethanol before and after exfoliation. The exfoliated Al-MOF nanosheets suspension was treated with a centrifugation process at 8,000 rpm for 15 min, and insignificant amount of non-exfoliated sediments were found. Photo credit: Meipeng Jian, Monash University.

Fig. S1A shows shows an overview of SEM micrograph of bulk-type Al-MOF crystals. Al-MOF bulks obtained by the solvothermal method display irregular morphologies. A close-up inspection of the crystals reveals that they actually consist of multiple, closely packed lamellae (Fig. 1A in the main text and Fig. S1B highlighted with yellow rectangles in the AFM image). The 3D crystalline structure of bulk Al-MOF consists of Al node with an octahedron

coordination geometry interconnected by H_2TCPP ligands. Each porphyrin linker is coordinated to 8 Al nodes. Two axial OH^- bridging adjacent Al coordination forms the infinite $Al(OH)O_4$ chain motif along (001) plane, resulting in multiple space groups of *C222*, *Cmm2*, and *Cmmm.* The constituting layers stack along the [001] crystallographic direction, forming the 3D bulk-type architecture (Fig. S1C). Nevertheless, the coordination bonds along [001] direction are weak and can be broken during the sonication treatment, forming 2D Al-MOF nanosheets. Fig.S1D shows the change of Al-MOF dispersions before and after the sonication exfoliation, apparently, the Al-MOF suspension becomes more dispersed (right) than that of Al-MOF bulks (left) after the exfoliation, signifying the successful exfoliation. Moreover, the concentration of the sample supernatant after the exfoliation was very high, after a high-speed centrifugation. This confirms the high exfoliation efficiency. Detailed exfoliation rates were quantified according to the mass discrepancy. The calibration standard curve has been built in Fig. S2D,E.

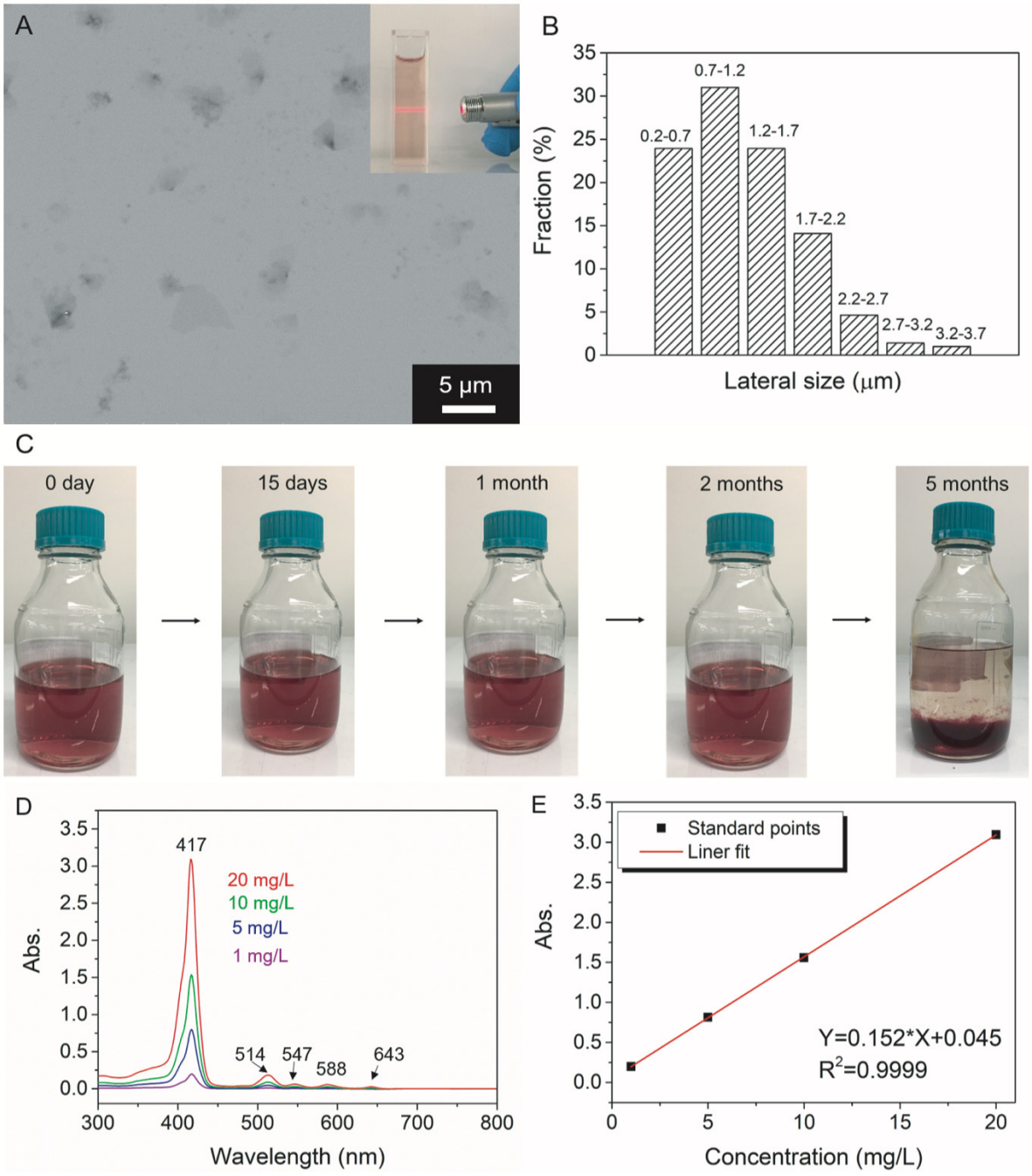

Fig. S2. Exfoliated Al-MOF nanosheets. (**A**) Backscattered SEM image of the exfoliated Al-MOF nanosheets on a silicon wafer. The inset shows a Tyndall effect of Al-MOF nanosheet colloidal suspension. (**B**) Frequency histogram of the corresponding lateral size of Al-MOF nanosheets. The sizes of these Al-MOF nanosheets were measured with the Image J software. In general, the sheets are irregularly shaped. For this reason, we estimated the lateral dimension along the longer axis and designated this as the lateral size. To ensure the accuracy, 100 sheets from SEM images were counted. (**C**) Dispersity change of Al-MOF nanosheets in ethanol solution with standing time. The concentration of Al-MOF nanosheet suspension was 2 mg/mL. (**D**) UV-Vis absorption spectra of Al-MOF nanosheet standard solutions. (**E**) Calibration standard curve of Al-MOF nanosheet dispersions using their UV-Vis absorption at 417 nm. Photo credit: Meipeng Jian, Monash University.

Fig. S2A evidences the success of exfoliated Al-MOF nanosheets. In contrast to bulk Al-MOF, well-defined nanosheets were observed. A Tyndall light-scattering effect was observed by a side-incident light beam, confirming the homogeneous Al-MOF sheets dispersion (Fig.S2A inset). The exfoliated Al-MOF nanosheets exhibited a quite broad lateral dimension ranging from 200 nm to a few microns. More importantly, Al-MOF nanosheets have excellent solubility in polar solvent of ethanol after sonication, even at the concentration of up to 2 mg/mL. The high solubility can maintain at least 2 months, but they tend to self-aggregate, ending up in settlements in the fifth month (Fig. S2C). The good solubility of Al-MOF nanosheets makes them ideal building blocks for defect-free membranes. UV-Vis spectrometry can be used to quantify the concentration of Al-MOF nanosheets in the solution. As Al-MOF shows a few bands at different wavelengths, the intensity of these bands (particularly at 417 nm) increases linearly with an increase in the concentration of Al-MOF nanosheets.

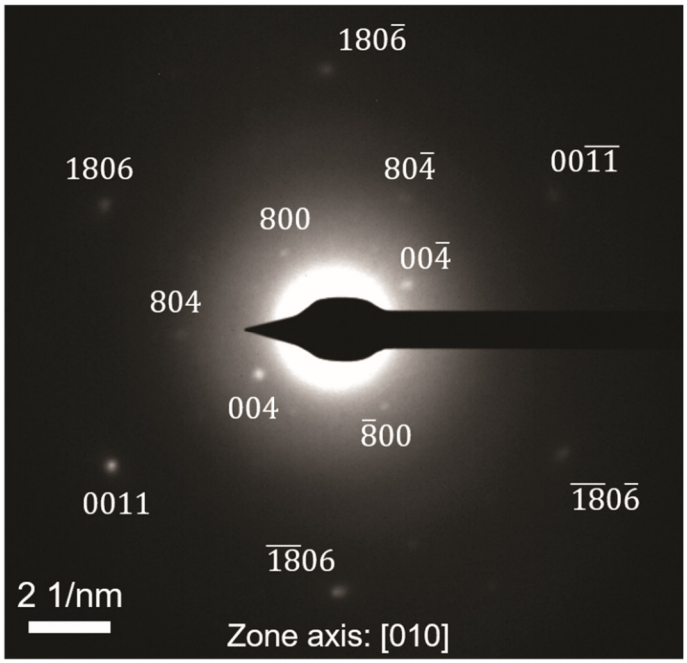

Fig. S3. SAED pattern of single-layer Al-MOF nanosheet. The SAED pattern gives individual diffraction spots, demonstrating the single crystal nature of the exfoliated Al-MOF nanosheet.

Fig. S3 presents the selected area electron diffraction (SAED) pattern of a single-layer Al-MOF nanosheet through the TEM characterization. The SAED pattern acquired a few diffraction spots with a [010] viewing zone axis, where individual diffraction spots are indexed to an orthorhombic phase that attributed to single-crystal Al-MOF.

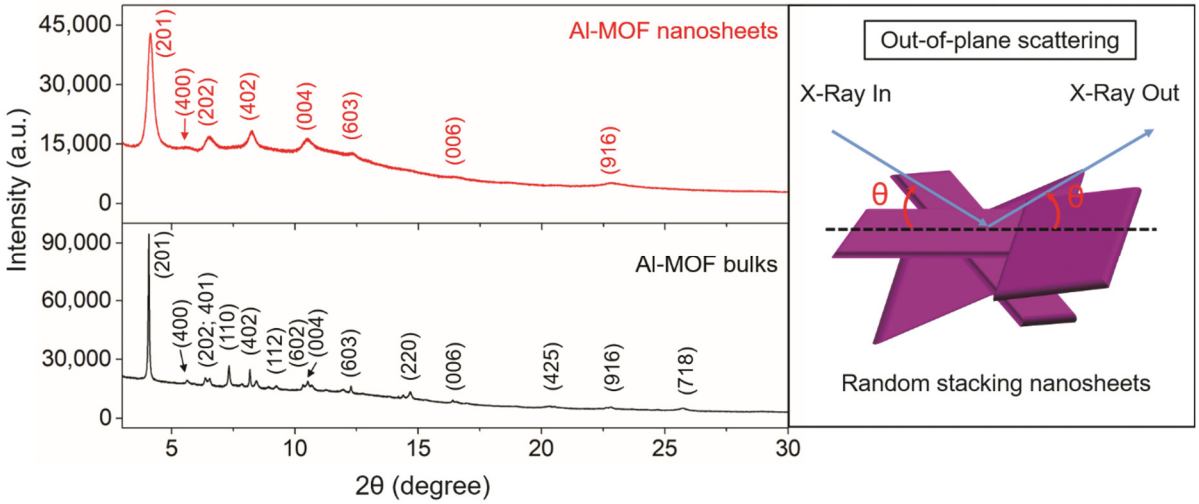

Fig. S4. XRD patterns for Al-MOF bulks and nanosheets. The observed XRD profile of Al-MOF nanosheets was recorded by stacking randomness as depicted in right inset.

The crystallinity of Al-MOF before and after sonication exfoliation was analyzed by synchrotron XRD. The exfoliated sheets exhibit weakened peaks and some broad bands disappear, such as (400), (110), (112) and (220) etc. facets. This is caused by the loss of diffraction signal in the out-of-plane direction (right inset), and the non-planar shape of the nanosheets (*24*). Since the XRD solid sample for Al-MOF nanosheets are randomly oriented on the XRD specimen disc, most notable peaks, such as (201), (202), (402) and (603) etc. therefore still retain. Thus, the XRD result provides the evidence of the formation of the nanosheets.

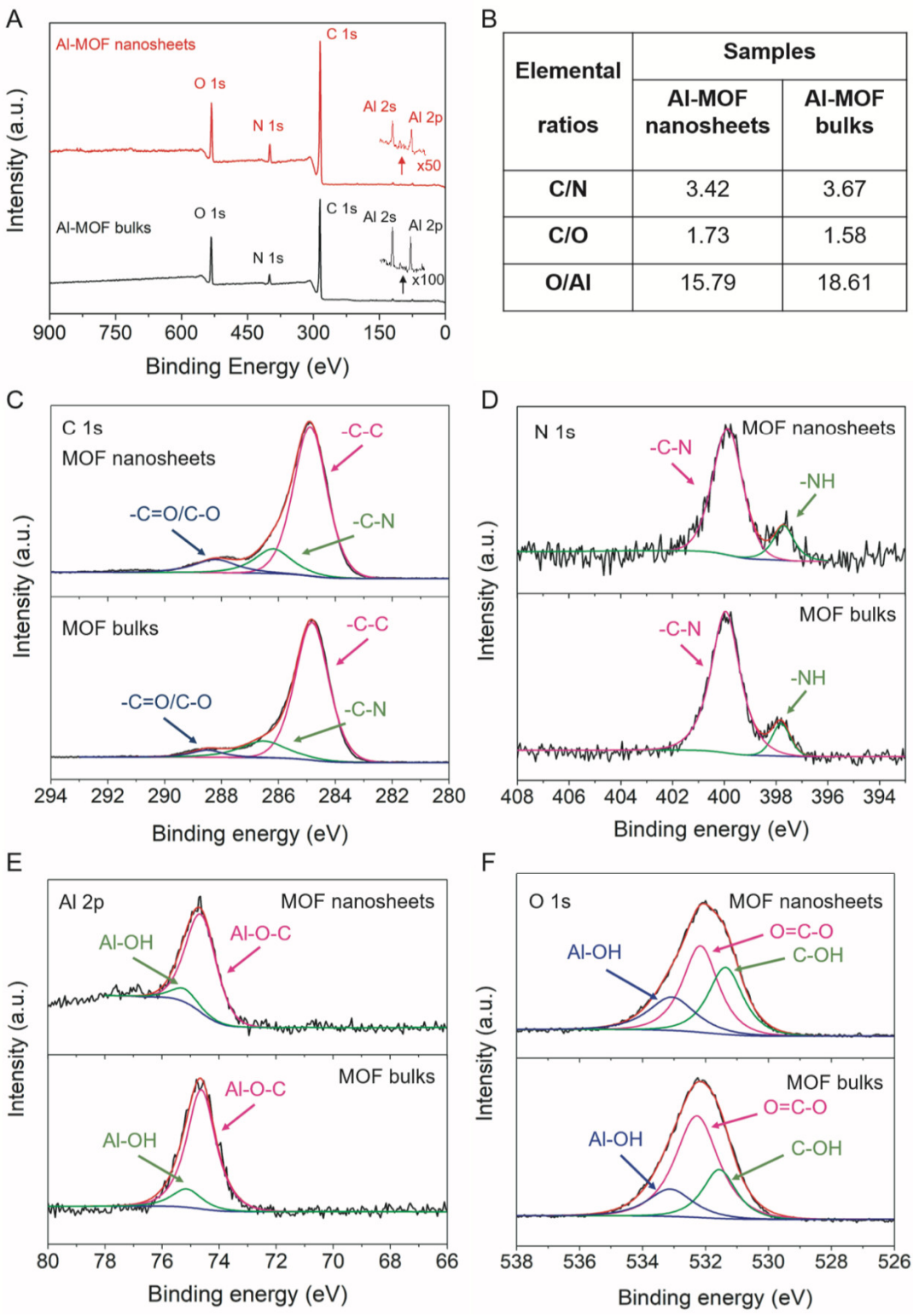

Elemental ratios	Samples	
	Al-MOF nanosheets	Al-MOF bulks
C/N	3.42	3.67
C/O	1.73	1.58
O/Al	15.79	18.61

Fig. S5. XPS spectra of the Al-MOF nanosheets and bulks. (**A**) survey scan (**B**) comparison of elemental ratios between Al-MOF nanosheets and bulks obtained by XPS analysis (**C**) C 1s (**D**) N 1s (**E**) Al 2p and (**F**) O 1s.

The elements of Al-MOF crystals before and after exfoliation were studied by XPS. The presence of Al, C, N, O was evident from both spectra, indicating the intact composition after sonication treatment (Fig. S5A). Additionally, the atomic ratios from XPS between individual elements (such as C/O; C/N, O/Al etc.) are also close before and after exfoliation (Fig. S5B).

Moreover, Fig. S5C-F show the high-resolution XPS spectra of C 1s, N 1s, Al 2p and O 1s core level peak regions for Al-MOF nanosheets and bulks. As shown in Fig. 5C, the C 1s peak centered at 284.9 eV is typically assigned to C-C and C=C from porphyrin ligand ring, whereas the C 1s peak at 286.2 eV is originated from sp^2 C atoms bonded to N and NH groups. The highest energy in C 1s at 288.2 eV is the contribution from the carboxyl group. After the exfoliation, the carboxyl group signal for Al-MOF nanosheets became stronger with respect to that of bulk-type Al-MOF. This could be attributed to that the Al-O nodes interacted with neighbouring layers are broken and O=C are attached on porphyrin ligand side re-coordination into HOOC after the exfoliation. Consistently, C-OH at 531 eV in O 1s spectrum of Al-MOF nanosheets has a larger area than that of Al-MOF bulks (Fig. S5F). Meanwhile, the N 1s peaks at 340 eV (-C-N) and 397 eV (-NH) from porphyrin ring in Fig. S5D remain consistent before and after exfoliation. Similarly, negligible change was observed in Al 2p spectra (Fig. S5E). These results signify the similar chemical composition and the coordination geometries between the exfoliated sheets and bulk-type Al-MOF.

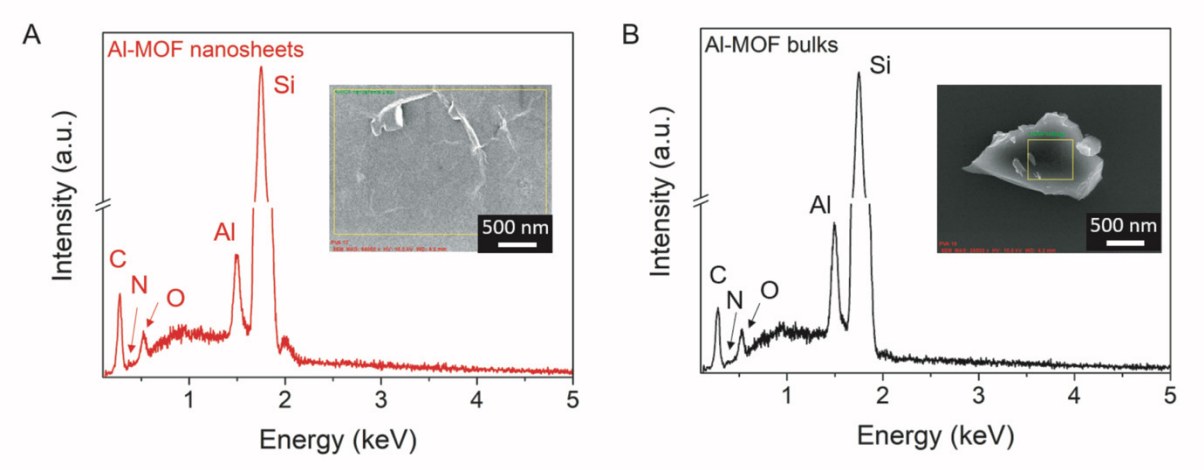

C

Element	Al-MOF nanosheets		Al-MOF bulks	
	Weight %	Atomic %	Weight %	Atomic %
C	8.11	18.55	8.39	17.45
N	0.64	1.11	0.40	0.72
O	1.09	1.66	1.05	1.64
Al	1.21	1.10	1.63	1.50
Si	88.95	77.58	88.53	78.69

Fig. S6. SEM-EDX spectra of the Al-MOF nanosheets and bulks. (**A**) Al-MOF nanosheets and (**B**) Al-MOF bulks. Inset depicts the scanning area on the corresponding sample. (**C**) Summarized table for the weight and atomic ratio of elements from Al-MOF nanosheets and bulks using Brüker Esprit software. Please note that Si count originates from the silicon wafer support. Photo credit: Meipeng Jian, Monash University.

The results show that no significant difference in the components between Al-MOF nanosheets and bulks.

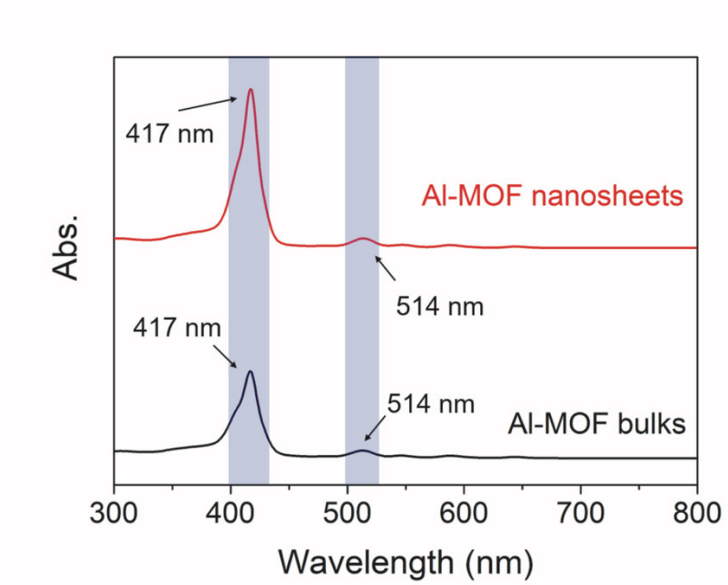

Fig. S7. UV-Vis spectra of Al-MOF nanosheets and bulks. Both samples were suspended in ethanol solvent.

The characteristic peaks (at 417 nm and 514 nm) of Al-MOF crystals were observed on both samples. Moreover, the absorbance peaks at the vital wavelengths did not take any shift, manifesting the identical structural coordination.

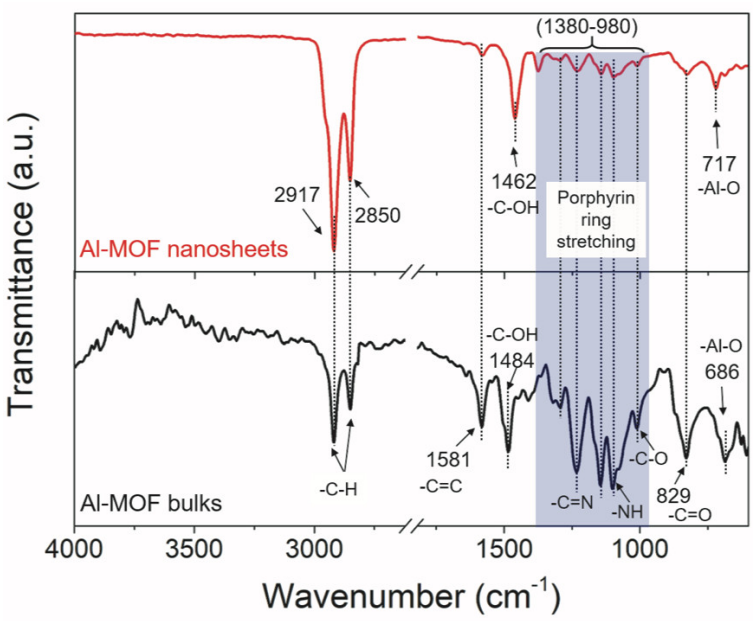

Fig. S8. FTIR spectra of Al-MOF nanosheets and bulks.

Most of FTIR characteristic peaks of Al-MOF nanosheets are similar to those of Al-MOF bulks. The peak at 829 cm^{-1} is associated to the deformation ν(C=O) (*36*). The convoluted bands at 980-1325 cm^{-1} are attributed to the entire porphyrin ring stretching including ν(C-O), ν(C=N) and ν(N-H) from H_2TCPP ligand (*37*). The peak at 1581 cm^{-1} is assigned to the –C=C from H_2TCPP ligand. The adsorption peaks at 2850 cm^{-1} and 2917 cm^{-1} represent the C-H symmetric stretching. Noticeably, Al-OH stretching vibrations in Al-MOF nanosheets after exfoliation was shifted from 686 cm^{-1} to 717 cm^{-1} (*38*). Meanwhile, C-OH bending peak at 1484 cm^{-1} in bulk-type Al-MOF was shifted to 1462 cm^{-1} in Al-MOF nanosheets. These characteristic variations result from the demolishing the interlaminar Al-OOC connections of Al-MOF bulks into Al-MOF nanosheets.

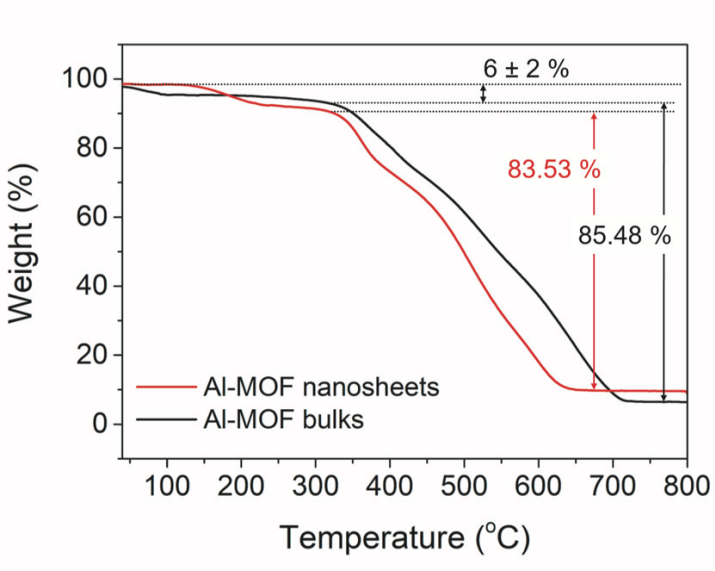

Fig. S9. TGA curves of Al-MOF nanosheets and bulks.

TGA data of Al-MOF bulks and nanosheets were collected under air heating procedure (10 °C/min). Both samples first experienced a slight weight loss (approximately 6 ± 2 %) before 320 °C, which is attributed to the loss of free water molecules that is bonded to the TCPP ligand group and unsaturated Al clusters of Al-MOF *via* H-bonds. The typical weight loss of Al-MOF bulks and nanosheets was determined to be 85.48 wt.% and 83.53 wt.% starting at 320 °C, respectively, which attributed to the removal of the organic ligands and structural decomposition. The results show that Al-MOF nanosheets exhibit a similar thermal stability to Al-MOF bulks.

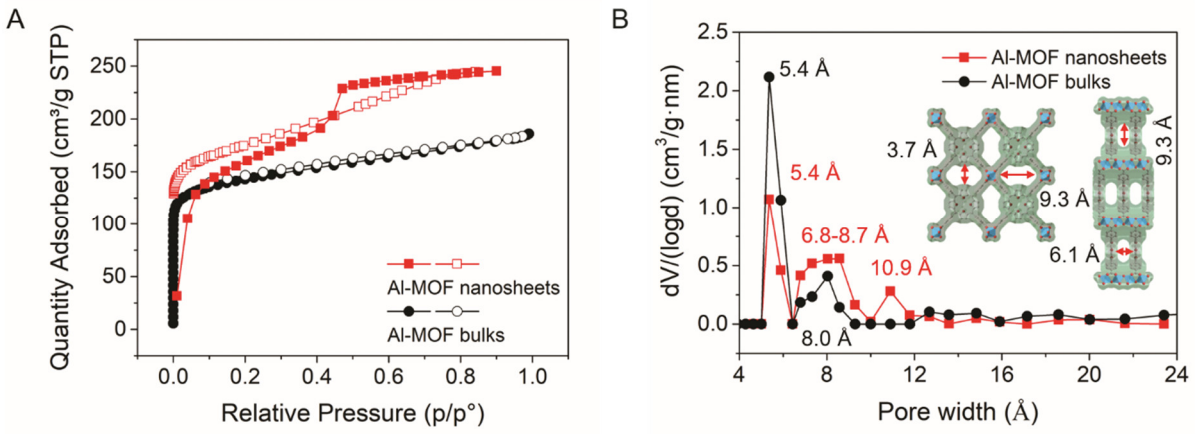

Fig. S10. Porosity characteristics of Al-MOF nanosheets and bulks. (**A**) N_2 adsorption-desorption isotherms and (**B**) the corresponding pore distributions of Al-MOF bulks and nanosheets. Insets showing the simulated elliptical pores (9.3×3.7 Å) viewed down [010] and rectangular pores (9.3×6.1 Å) viewed down [001] direction, which are calculated with 1.4 Å Van der Waals scale factor.

Al-MOF nanosheets feature microporous structure (a type-I isotherm curve) and have a specific surface area of 602 m^2 g^{-1}, which is higher than that of the bulk (431 m^2 g^{-1}). Given the additional slit-like pores by inevitable restacking of dried nanosheets sample, a hysteresis loop appears and the pore distribution of Al-MOF nanosheets becomes diversified (Fig. S10A). On the other hand, the pore sizes of both samples are both narrowly distributed in micropore range, meaning a negligible change for Al-MOF nanosheets after exfoliation (Fig. S10B). In details, the data were extracted from Barrett-Joyner-Halenda (BJH) method, where it considered the default pore is sphere-shape (*39*), Therefore, the most prominent peak at 5.3 Å pore width should be ascribed to the elliptical pore (3.7 by 9.3 Å [ellipse] ≈ 5.8 Å [circle] calculated by the area) as described in the left inset image. Secondly, 6.8-8.7 Å range should be directed to the rectangular pores (6.1 by 9.3 Å [rectangle] ≈ 7.8 Å [circle]) in the [001] direction. By contrast, compared to the result of bulk-type Al-MOF which is centralized at 8.0 Å, the plot in the range of 6.8-8.7 Å for Al-MOF nanosheets are more broad. This could be resulted from the exfoliation effect, in which some rectangular pores are expanded to be slit channels. Lastly, a new additional pore at 10.9 Å appears in a fairly low volume fraction in Al-MOF sheets, which might be caused by the nanosheets random aggregation effect.

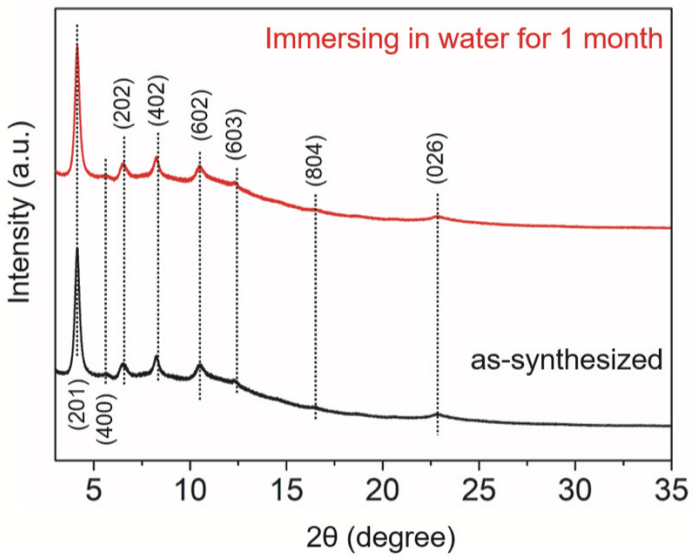

Fig. S11. Structural phase stability of Al-MOF nanosheets in water. XRD spectra of as-synthesized Al-MOF nanosheets before and after being immersed in water for a month at ambient temperature.

The positions of the Al-MOF nanosheets' characteristic peaks are basically identical as those of the original status, which confirms the crystalline stability of Al-MOF nanosheets in water.

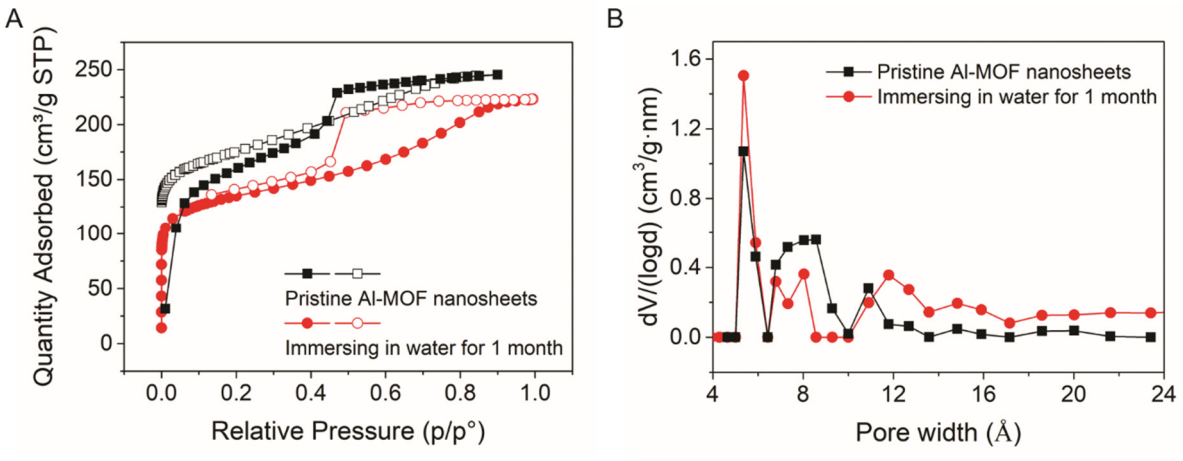

Fig. S12. Porosity retaining of Al-MOF nanosheets in water. (**A**) N_2 adsorption-desorption isotherms and (**B**) the corresponding pore distributions of Al-MOF nanosheets before and after immersed in water for a month.

Fig. S12A compares the nitrogen adsorption-desorption isotherms and the corresponding pore size distribution of both samples. In spite of immersed in water for one month, Al-MOF nanosheets still show high porous structure, presenting similar type-I isotherm with a typical hysteresis loop. The pore size distribution curves of the two samples display a similar trend (Fig. S12B). This confirms the retained porosity of Al-MOF nanosheets after in water for a month.

A

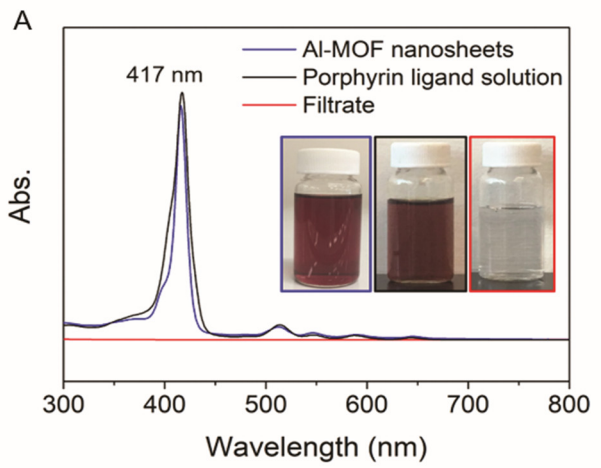

B

	Al-MOF nanosheets after immersing in water for 1 month
Theoretical Al^{3+} composition	46 mg/L
ICP test	Not detected

Fig. S13. Integrity assessment of Al-MOF nanosheets in water. (**A**) UV-Vis absorbance of the porphyrin ligand in water solution and the filtrate after Al-MOF nanosheets are removed *via* filtration with a 100 nm AAO filter. Insets are the corresponding photographs of solutions. (**B**) Summary of Al^{3+} leaching result of Al-MOF nanosheets after immersing in water for 1 month from ICP analysis. Photo credit: Meipeng Jian, Monash University.

Porphyrin ligand has a characteristic absorption peak at the wavelength of 417 nm, as shown in the UV-Vis spectra. The absence of the characteristic peak of porphyrin ligand in the filtrate (100 nm pore AAO filter) indicates that no porphyrin ligand was leached into the solution (Fig. S13A). Inset photograph additionally shows a clear solution after the filtration. Moreover, Al^{3+} leaking rate of Al-MOF nanosheets in water for one month was also examined through ICP analysis, as summarized in the Fig. S13B, Al^{3+} dissolution was not detected. These reveal the good water-stability of Al-MOF nanosheets.

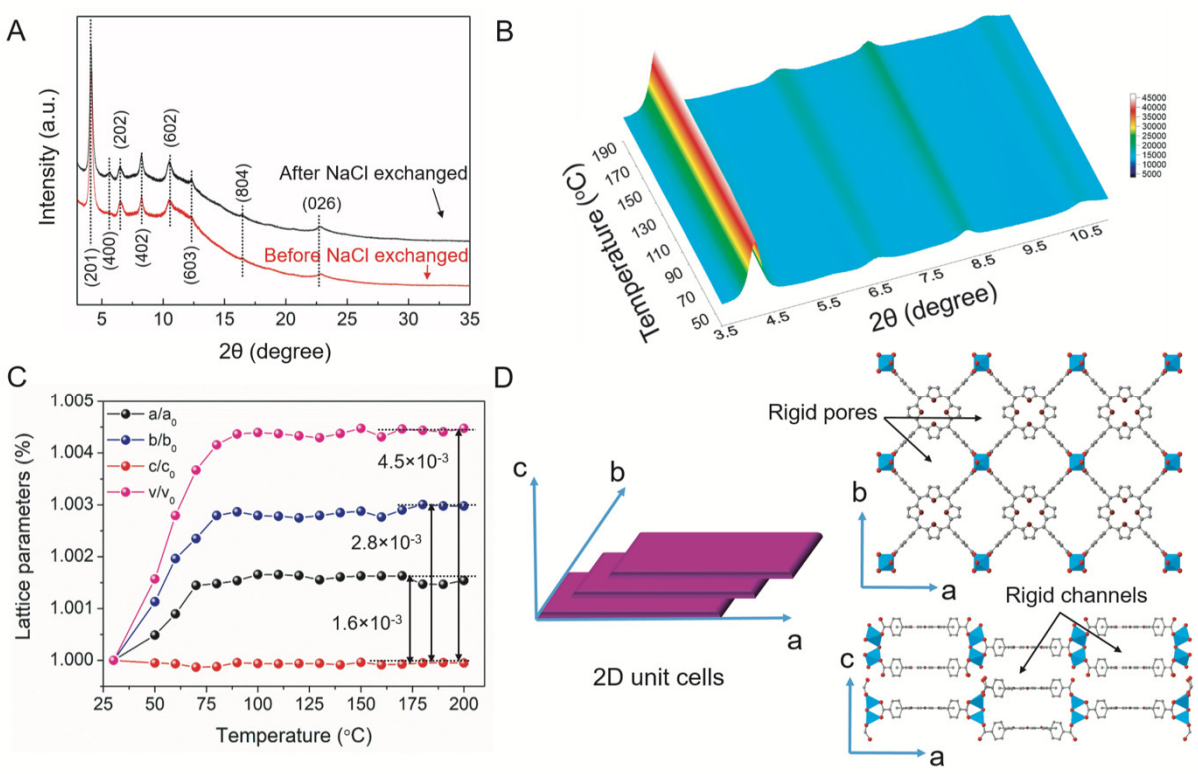

Fig. S14. Synchrotron XRD for confirming the rigidity of Al-MOF crystal structure and pore-apertures. (**A**) Comparison of XRD patterns of pristine Al-MOF nanosheets and treated Al-MOF nanosheets with 0.5 M NaCl for 24 hours; (**B**) 3D plot of in-situ XRD patterns of Al-MOF nanosheets as a function of the elevated temperature. (**C**) Rietveld refined lattice parameters of Al-MOF nanosheets from room temperature to 200 °C. (**D**) Definition of vectors (*a*, *b* and *c*) and description of the orientation of the Al-MOF nanosheet cell in real space. We use two vectors (*a* and *b*) to represent both the lengths and directions of the cell edges, whereas vector *c* is marked as a translational displacement in the adjacent layers stacking.

The NaCl exchange treatment with Al-MOF nanosheets was performed by adding Al-MOF nanosheets powder (10 mg) into a NaCl solution (0.5 M, 10 mL), as described in the section of "Salts adsorption capacity on Al-MOF nanosheets" in Materials and Methods. The NaCl exchanged Al-MOF nanosheets shows almost identical lattice indexing features to those of the pristine Al-MOF nanosheets (Fig. S14A). This suggests that the salt exchange process did not deteriorate the structure and the overall stability of Al-MOF nanosheets. Furthermore, the lattice phase of Al-MOF nanosheet remains constant with increasing temperature, as plotted in the Fig. S14B. Besides, we measured the temperature dependence of the lattice parameters of Al-MOF nanosheets (Fig. S14C). The lattice of *c* kept nearly unchanged over the entire measured temperature range, whereas the change of *a* and *b* lattices with temperature increasing is insignificant, being about +0.15 % and +0.28 %, respectively. Thus, the overall lattice volume variation is lower than 0.50 % along with the temperature. This shows an excellent pore rigidity of Al-MOF nanosheets under the thermal expansion (Fig. S14D). In summary, the structural and pore rigidity of the Al-MOF nanosheets are confirmed by using both salt exchange treatment and *in-situ* XRD at variable-temperature.

Fig. S15. Photograph of Al-MOF nanosheet dispersion in water for membrane preparation. The concentration is 1 mg/L. Photo credit: Meipeng Jian, Monash University.

We purposely diluted the original dispersion from 2 mg/mL to 1 mg/L by adding deionized water, which slowed down the membrane assembling process to avoid the formation of defects (*40*). Please be noted that the solubility of diluted Al-MOF nanosheets suspension by water is as good as that in ethanol.

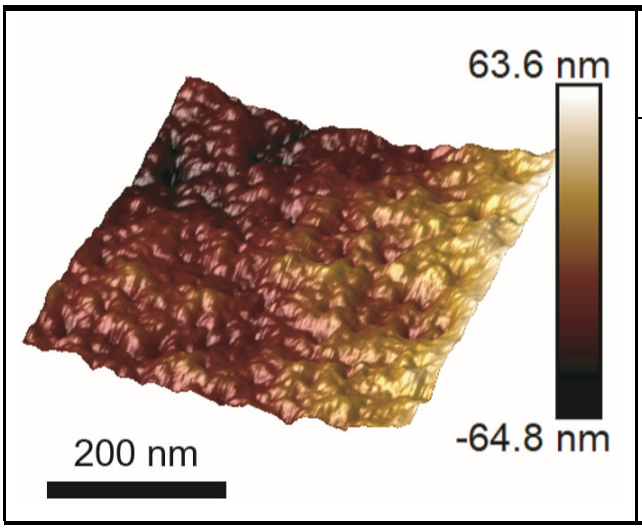

	Al-MOF membranes
Rq (nm)	10.30
Ra (nm)	8.25

Fig. S16. AFM characterization of Al-MOF membrane. AFM image of the top surface of 100 nm-thick Al-MOF membrane. The right table shows the surface roughness parameters of the membrane.

Fig. S16 shows the AFM surface topography of the Al-MOF membrane in a tapping mode. AFM displays a low surface roughness of 8.25 nm for the Al-MOF membrane (the right table), indicating that the well-aligned deposition of Al-MOF nanosheets laid on flat substrates.

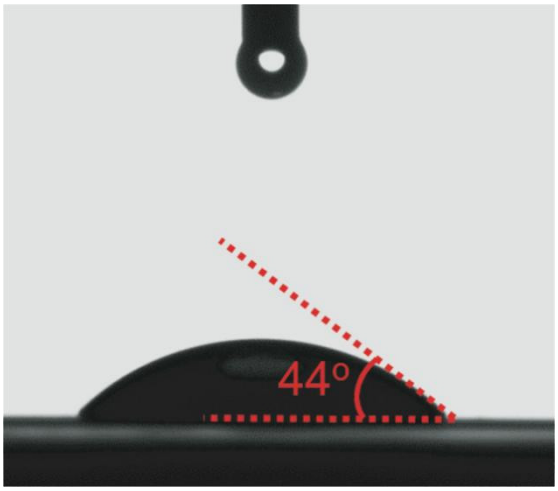

Fig. S17. Contact angle of Al-MOF membrane.

The surface wettability of Al-MOF membrane was examined through measuring water contact angles. Al-MOF membrane shows a hydrophilic nature evidenced by a contact angle of 44°.

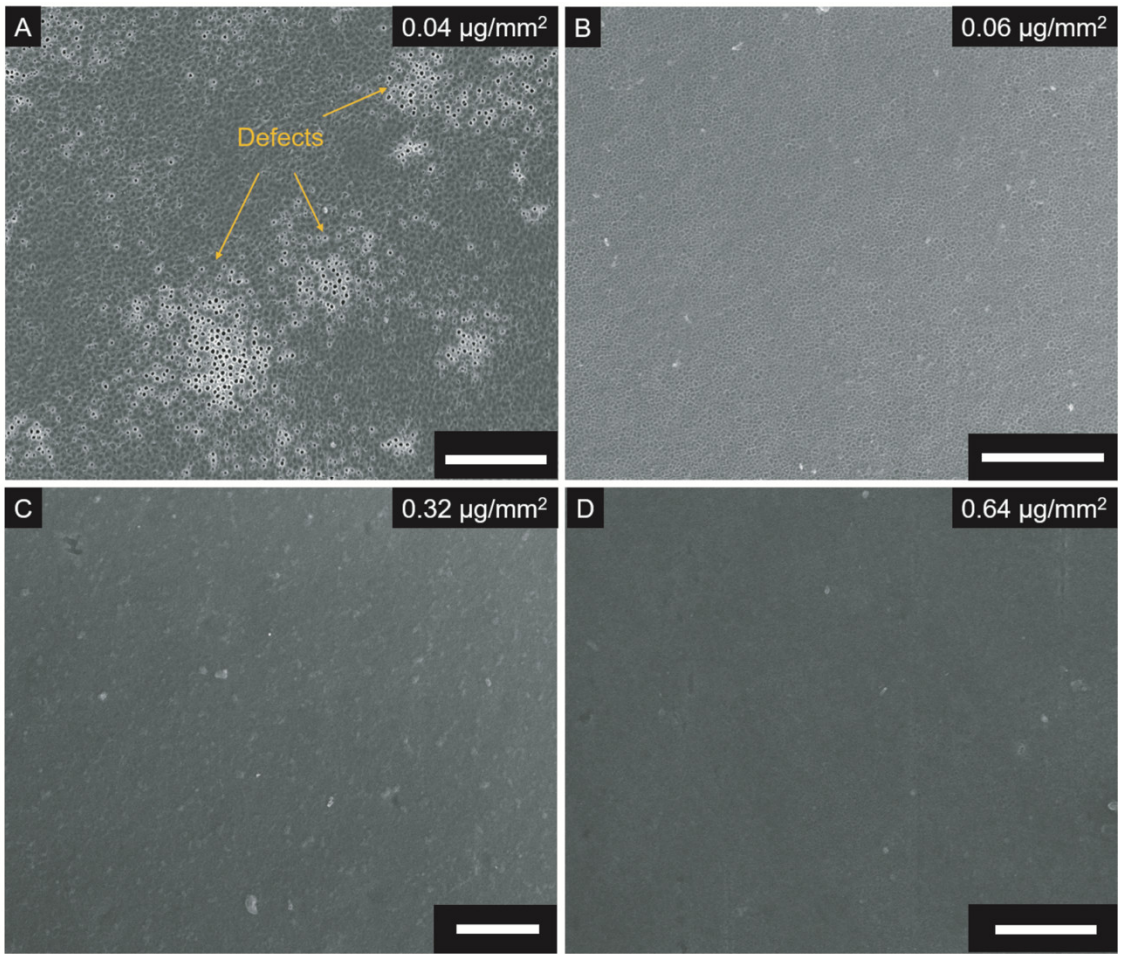

Fig. S18. Optimization of Al-MOF nanosheet loadings for the membranes. SEM surface images of 2D Al-MOF membranes with different nanosheet loadings including (**A**) 0.04, (**B**) 0.06, (**C**) 0.32 and (**D**) 0.64 µg/mm^2. Scale bars: 5 µm.

After filtration of Al-MOF nanosheet suspension with an anodized alumina (AAO) substrate (Anopore, pore size 100 nm), a uniform, well-packed deposit layer consisting of highly oriented, overlapping, flat nanosheets can be formed. Fig. S18 displays a top-view SEM images of Al-MOF nanosheets deposited on AAO substrates. When the Al-MOF nanosheet loading is below 0.04 µg/mm^2, there is a low coverage of sheets on the substrate and visible defects are visible (Fig. S18A). Uniform surface coverage can be observed when the loading reaches 0.06 µg/mm^2. Because the nanosheets are very thin, the porous AAO substrate background can still be seen (Fig. S18B). In the meantime, no defects such as cracks and pinholes are visible. With increasing the loading, the surface becomes denser and more compacted gradually (Fig. S18C, D).

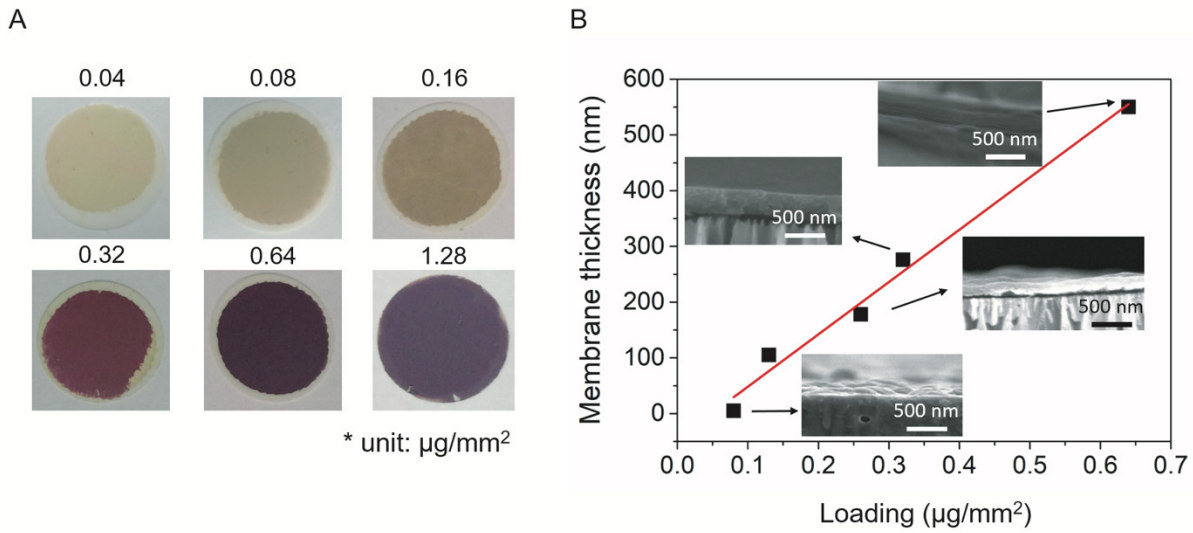

Fig. S19. Al-MOF membranes with different nanosheet loadings. (**A**) Digital photos of the prepared Al-MOF membranes on AAO substrates with different nanosheet loading (μg/mm^2). (**B**) Correlation between the membrane thickness and the loading of Al-MOF nanosheets. Photo credit: Meipeng Jian, Monash University.

It can be seen that the color of Al-MOF membranes changes from light brown to purple with an increase in the nanosheet loading (Fig. S19A). The membrane thickness has a liner relationship with the loading, which is plotted in the Fig. S19B.

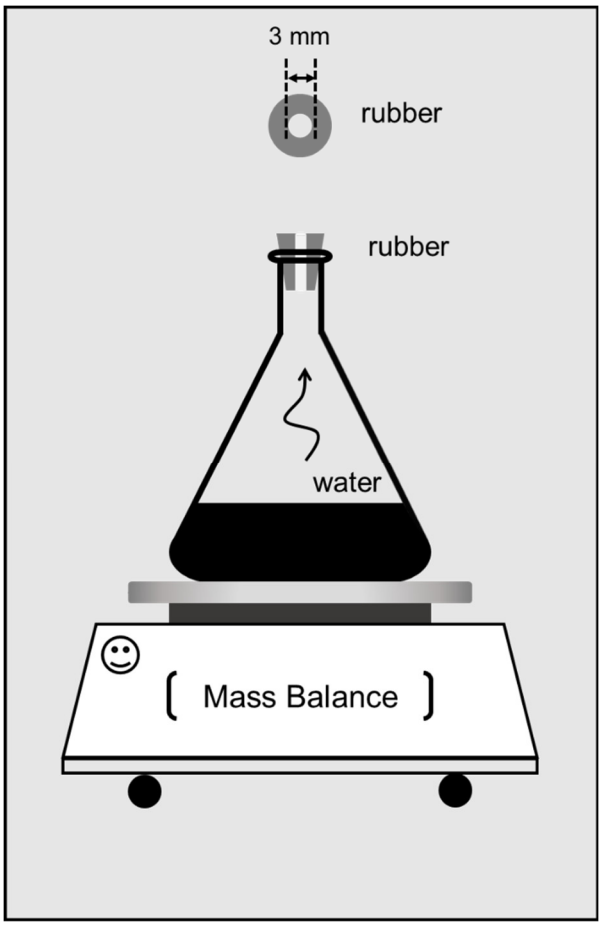

Fig. S20. Schematic of water evaporation experimental setup.

Fig. S20 shows the apparatus of this test, where a 100 nm thick Al-MOF membrane was sealed onto the top rubber through water-proof glue and a fixed volume of water liquid (75 mL) was filled in the flask container (250 mL size). The evaporation weight loss experiment was also conducted in the absence of the Al-MOF membrane (it refers to the open aperture) as a control. Similar water evaporation rates were observed from the container sealed with a pristine membrane and with an open aperture (Fig. 3A in the main text).

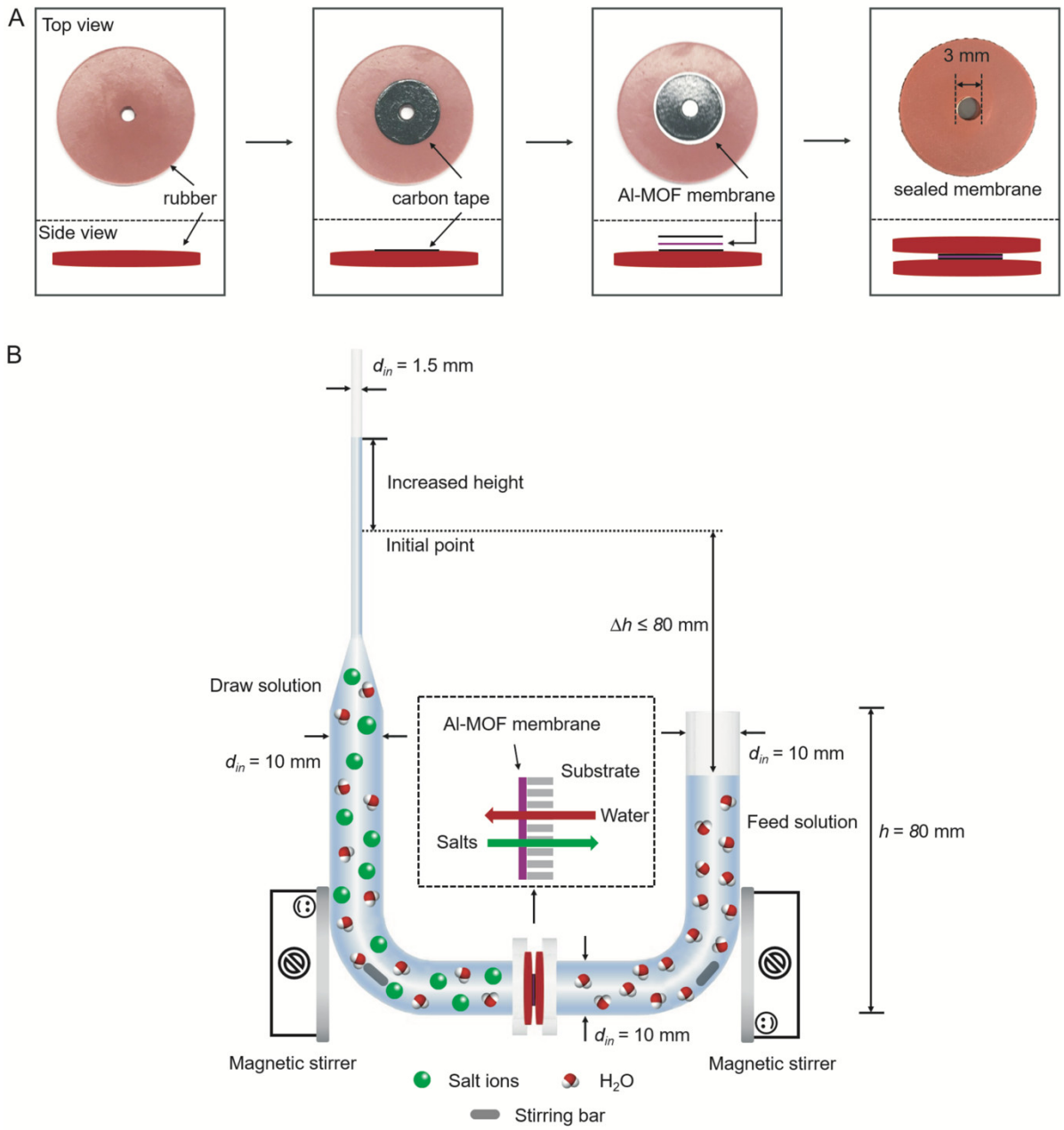

Fig. S21. Illustration of the ion permeation through Al-MOF membranes. (**A**) Schematic of mechanical sealing of Al-MOF membranes for the diffusion test. Step 1: Punch a 3 mm pore across a rubber. Step 2: Stick a double-adhesive and water-proof carbon tab with 3 mm punched pore on the above rubber. Step 3: Transfer of an as-prepared Al-MOF membrane (face to bottom) onto the carbon tab. Another punched carbon tab was attached onto the membrane. Step 4: Another punched rubber stick on the top. (**B**) Schematic of the diffusion apparatus, which is driven by the osmotic pressure of draw solutions. Considering the visible permeation process in the liquid level at draw side, we reformed the draw compartment with 1.5 mm inner diameter at the top. The height difference is controlled within 80 mm, that is the equivalence of 7.85 millibar, therefore, can be neglected. Photo credit: Meipeng Jian, Monash University.

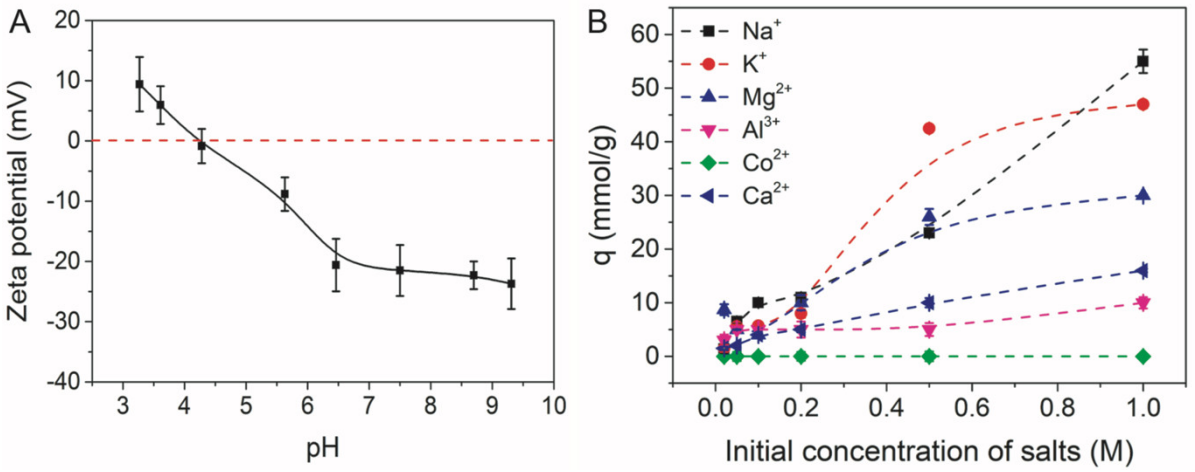

Fig. S22. Ion affinity onto Al-MOF nanosheets. (**A**) Zeta potential of Al-MOF nanosheets in water. (**B**) Adsorption isotherms of different salt ions on Al-MOF nanosheets.

As shown in Fig. S22A, the isoelectric point of Al-MOF nanosheets is measured to be around 4.2, meaning Al-MOF nanosheets are negative charged when solution is at neutral pH. In principle, cations tend to adsorb on the Al-MOF nanosheets because of the electrostatic attraction at the neutral condition. Fig. S22B summarized the adsorption isotherms of different salts on Al-MOF nanosheets in water at neutral pH at ambient temperature. We can see that Na^+, K^+ ions lead an adsorption equilibrium at roughly 45 mmol/g. The adsorption capacity follows a decrease tendency with the sequence of Mg^{2+}, Ca^{2+} and Al^{3+}. In a sharp contrast, Co^{2+} ions exhibited a low adsorption on Al-MOF nanosheets.

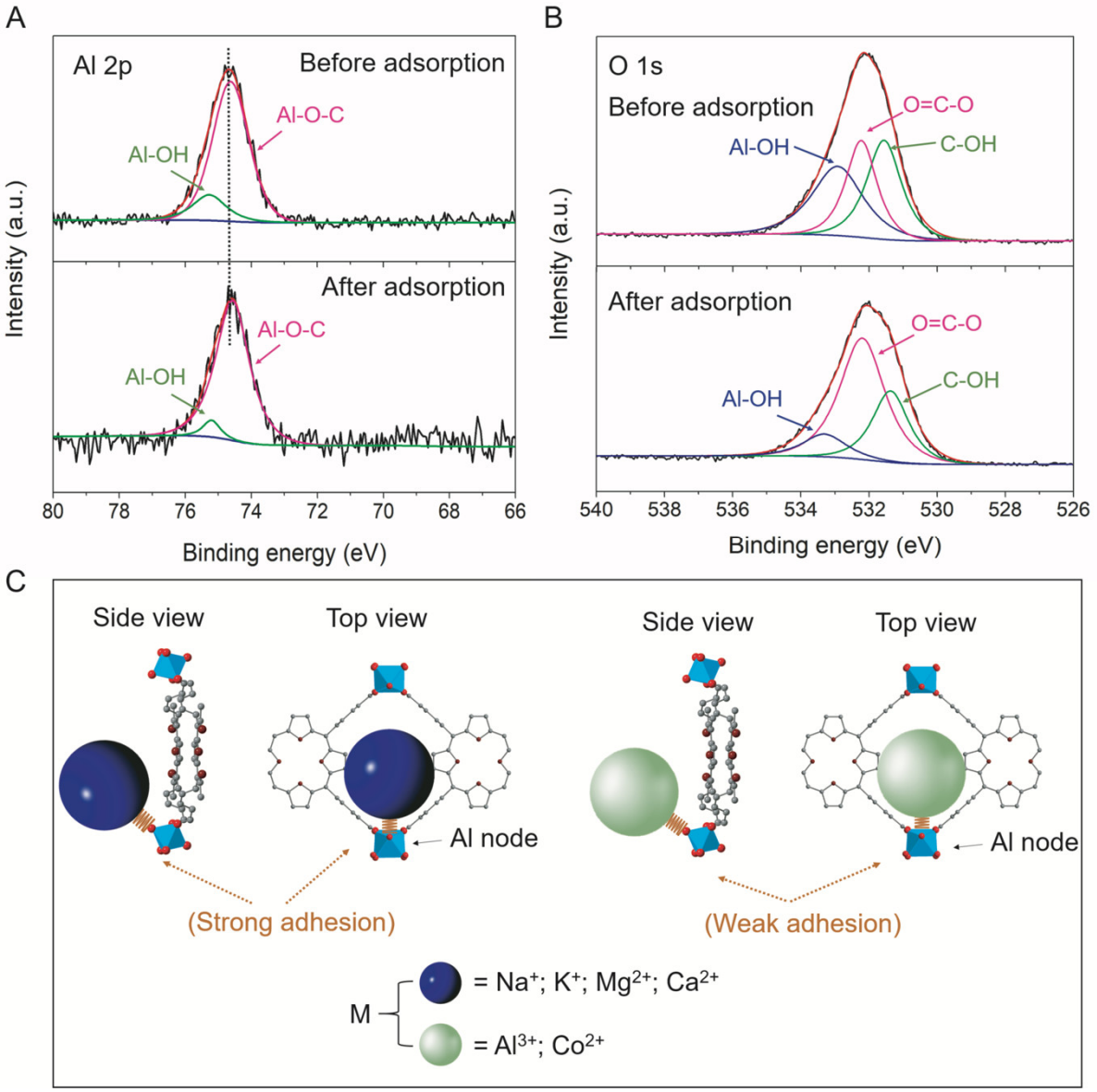

Fig. S23. High-resolution XPS spectra of Al-MOF nanosheets before and after NaCl adsorption. (**A**) Al 2p and (**B**) O 1s. (**C**) Schematic illustration of the adsorption capacities for various cations on Al-MOF crystal apertures.

Based on the above adsorption experiments, we found that the unsaturated surface Al hydroxyl groups on Al-MOF nanosheets serve as active sites for cations adsorption, as confirmed by XPS results. As shown in Fig. S23A, the Al 2p spectra slightly shifted to a lower energy after loaded with NaCl, implying that Al was involved in the salt sorption. Meanwhile, the peak at binding energy of 533.3 eV that assigned to Al-OH in O 1s spectra became significantly weaker after adsorption (Fig. S23B). These results reveal that the surface aluminum hydroxyl groups on Al-MOF nanosheets play a vital role in the salts adsorptive process. Combined with experimental results from Fig. S22, the adsorption capacities for various cations on Al-MOF crystal apertures have been illustrated in Fig. S23C.

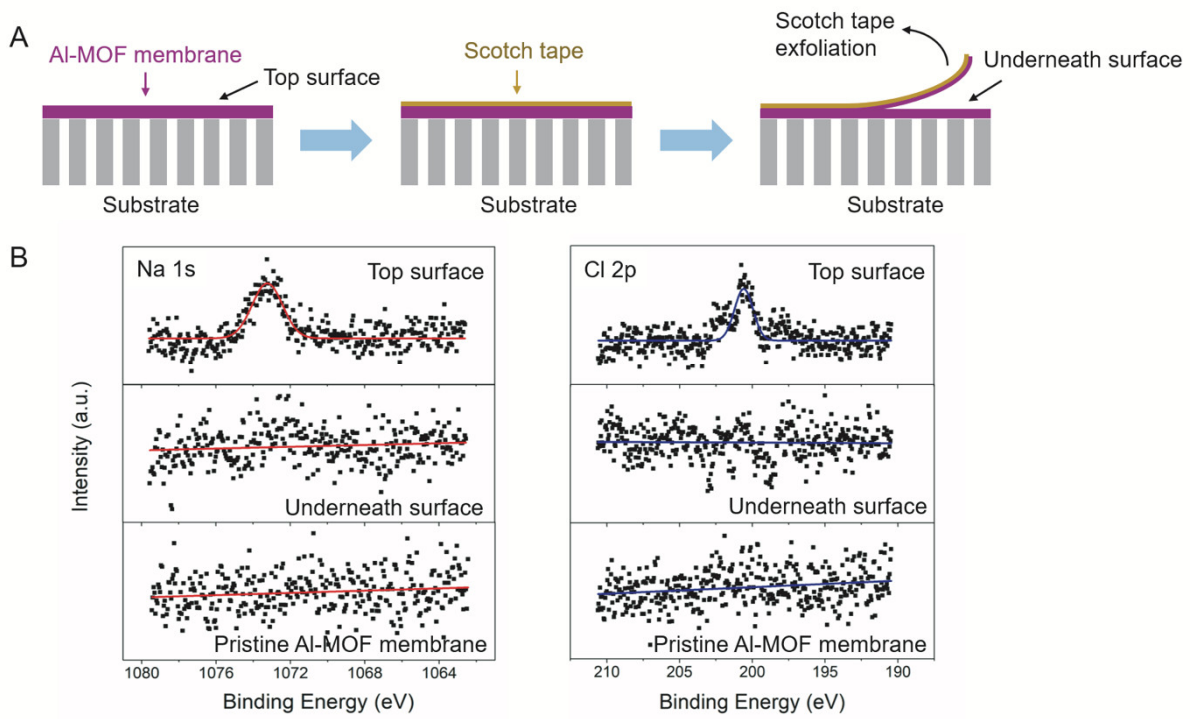

Fig. S24. XPS analysis for Al-MOF membranes after NaCl permeation. (**A**) Schematic diagrams of Al-MOF membranes for XPS analysis. Considering the vulnerability of AAO substrate for the tape-exfoliation process, we replaced it with a PES polymer substrate in this characterization. Step 1: A dried Al-MOF membrane on PES substrate after 24 hours NaCl permeation test. Step 2: Cover a single-adhesive Scotch tape on the top of Al-MOF membrane. Step 3: Slightly exfoliate the membrane from the substrate by pulling tape up. (**B**) XPS spectra of Na 1s and Cl 2p on an Al-MOF membrane with different depths before and after NaCl permeation.

To demonstrate the ion pathway through Al-MOF membranes, XPS analysis was performed to characterize the membrane at different depth levels before and after 0.5 M NaCl permeation. We observed the residual NaCl on the membrane surface after the 24 hours diffusion process, on the basis of Na 1s and Cl 2p peaks at 1073 eV and 201 eV, respectively. However, no XPS signal can be found underneath of the top membrane surface, signifying the insignificant amount of NaCl permeated through the membrane. This result is also consistent with the experiment results that the permeation of NaCl cross the membranes is almost negligible.

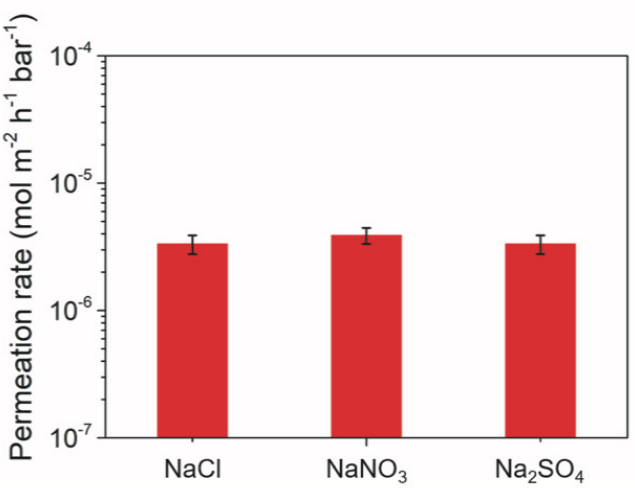

Fig. S25. Effect of different anions on Na^+ permeation rate. 0.5 M NaCl, $NaNO_3$ and Na_2SO_4 were used as the draw solution, respectively.

In addition, we further investigated the effect of anion species on the salt permeation. As shown in Fig. S25, the anion species have no apparent impact on salt permeation.

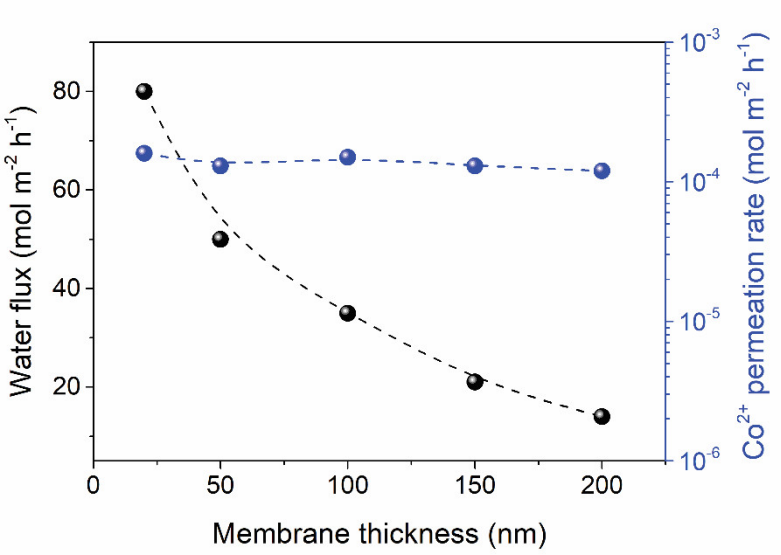

Fig. S26. Performances of Al-MOF membranes as a function of membrane thickness. 0.5 M Co^{2+} was used as the draw solution.

From the Fig. S26, it is clear that water flux can be significantly improved by decreasing the membrane thickness. As the thickness decreasing from 200 nm to 20 nm, the water flux of Al-MOF increases 8 times, and reaches to 2.22 mol m^{-2} h^{-1} bar^{-1}. Meanwhile, Co^{2+} permeation rate is essentially unaffected.

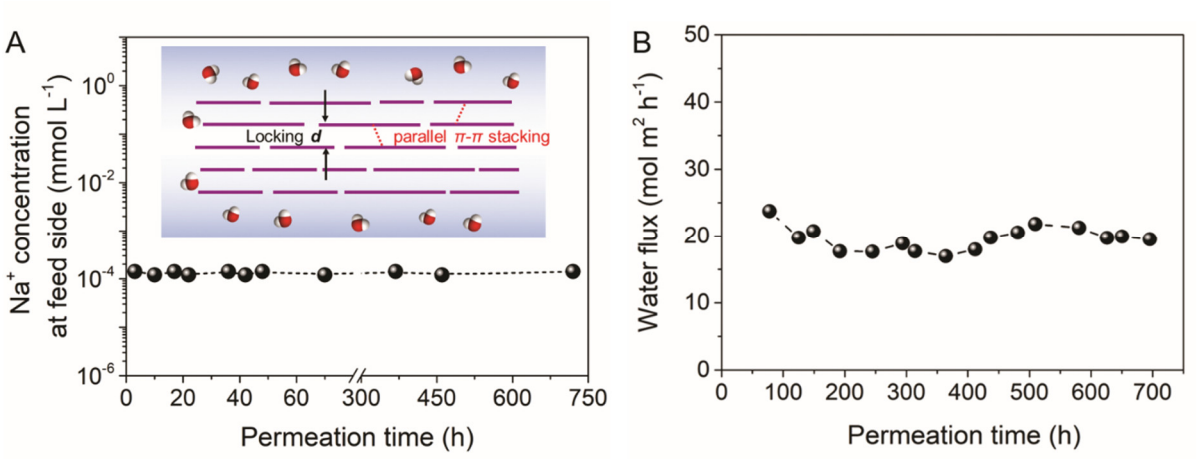

Fig. S27. Long-term performances of Al-MOF membranes. (A) Na^+ concentration change in the feed solution and (**B**) water flux of the Al-MOF laminar membrane as a function of time in a month diffusion running, 0.5 M Co^{2+} was used as the draw solution. The thickness of Al-MOF membrane is 150 nm.

As observed in Fig. S27A, Na^+ ion concentration at the feed side for the Al-MOF membrane remained almost unchanged after being diffusion in water for one month, showing an excellent anti-swelling ability and stability of the Al-MOF membrane in aqueous solution. This might be attributed to the locking effect of adjacent nanosheets by means of parallel π-π interaction (Fig. S27A inset). On the other hand, Fig. S27B further indicates the long-term stability of the Al-MOF laminar membrane, where a constant water flux over a month is achieved.

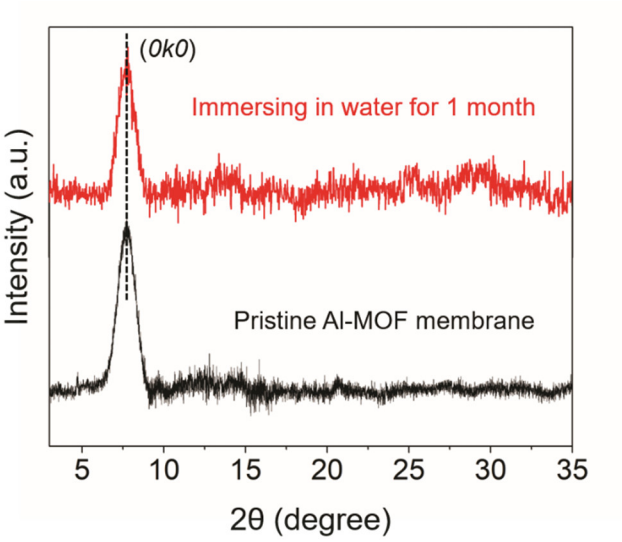

Fig. S28. Structural stability of Al-MOF membranes. GIXRD patterns of Al-MOF laminar membranes before and after immersing in water for a month.

It is evident from the comparison of Fig. S28 that the intense reflection (0k0) peak at $2\theta = 7.6^{o}$ for both Al-MOF membrane samples is almost identical with no shifts, after exposing the Al-MOF membrane to water for 1 month, which is indicative of their outstanding anti-swelling capacity towards water.

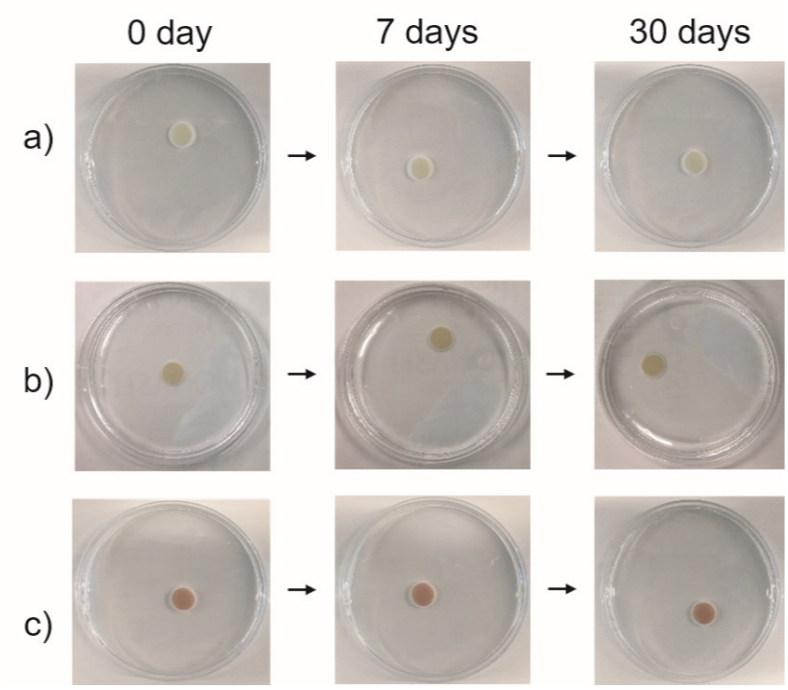

Fig. S29. Stability evaluation of Al-MOF membranes in water. Al-MOF membranes with different thicknesses (a: 100 nm, b: 200 nm and c: 500 nm) soaking in water for 30 days. Photo credit: Meipeng Jian, Monash University.

Fig. S29 includes a complementary set of photos from different thickness Al-MOF membranes in water for various periods. No dissolution or detachment from substrates of Al-MOF membranes was observed, showing the good stability of Al-MOF membranes in water. This observation also supports our findings that Al-MOF membranes can achieve a long-lasting efficient ion sieving in water.

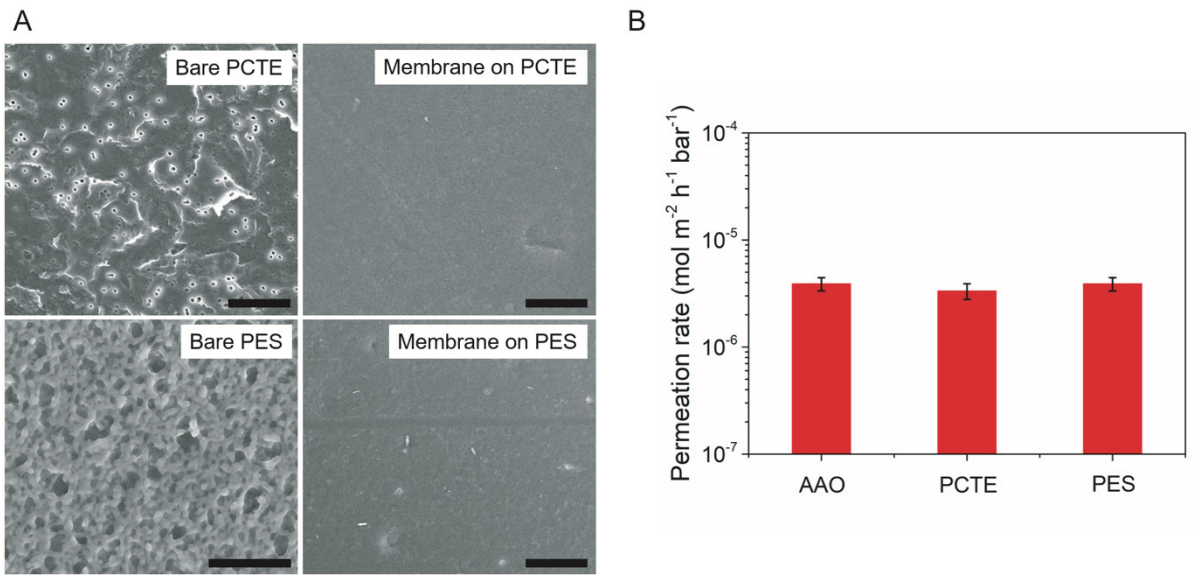

Fig. S30. Al-MOF membranes on polymer substrates. (**A**) Surface morphologies of 100 nm thick Al-MOF membranes on PCTE and PES substrates. Scale bars: 2 μm. (**B**) Different substrates effect on the reverse Na^+ permeation performances, the initial NaCl concentration is 0.5 mol L^{-1}.

In contrast, polymeric membranes display softer and flatter surface. Pristine PCTE substrate has uniformly distributed micropores with a nominal pore size of 20 nm, while the nodular structure can be found on PES substrate (Fig. S30A). After the deposition of Al-MOF nanosheets on both polymeric substrates, both were completely covered by Al-MOF nanosheets with a continuous membrane layer. Being different from the AAO substrates, the interfacial adhesion between Al-MOF sheets and polymeric substrates are stronger. The Na^+ permeation rate of Al-MOF membranes on polymeric substrates was also investigated. As anticipated, similar NaCl permeation rates were achieved as the membranes on AAO substrates (Fig. S30B).

Table S1. The comparison of state-of-the-art laminar membranes for water/ions separation in a diffusion cell.

Types	Membrane configuration	*$\Delta\pi_{theo}$ (bar)	J_w (mol m^{-2} h^{-1})	$J_w/\Delta\pi_{theo}$ (mol m^{-2} h^{-1} bar^{-1})	J_s (salt species) (mol m^{-2} h^{-1})	Selectivity (J_w/J_s)	Ref.
Reduced graphene oxide (rGO)	rGO	12	31.67	2.64	0.301 (NaCl)	105.2	(*41*)
	KCl-controlled rGO	12	12.22	1.02	0.063 (NaCl)	193.97	(*41*)
Graphene oxide (GO)	GO	25	27.78	1.11	0.428 (KCl)	64.9	(*11*)
	GO	25	27.78	1.11	0.214 ($MgCl_2$)	129.8	(*11*)
	Physically confined GO	48	n/a	n/a	0.005 (KCl)	n/a	(*42*)
	GO-280	12	47.22	3.94	0.900 (NaCl)	52.47	(*41*)
	KCl-controlled GO-280	12	20	1.67	4.8×10^{-3} (NaCl)	4.17×10^{3}	(*41*)
	GO-550	12	27.22	2.27	0.320 (NaCl)	85.06	(*41*)
	KCl-controlled GO-550	12	12.78	1.07	2.0×10^{-3} (NaCl)	6.39×10^{3}	(*41*)
	GO-750	12	9.44	0.79	0.190 (NaCl)	49.68	(*41*)
	KCl-controlled GO-750	12	5.56	0.46	2.7×10^{-4} (NaCl)	2.06×10^{4}	(*41*)
Molybdenum Disulfide (MoS_2)	Pristine MoS_2	25	80.5	3.22	n/a	n/a	(*43*)
	Crystal violet modified MoS_2	25	16.75	0.67	0.130 (NaCl; KCl)	128.85	(*43*)
	Crystal violet modified MoS_2	25	16.75	0.67	0.030 ($MgCl_2$)	558.33	(*43*)
	Crystal violet modified MoS_2	25	16.75	0.67	0.056 ($CaCl_2$)	299.11	(*43*)
	Sunset yellow modified MoS_2	25	39	1.56	0.150 (NaCl)	260	(*43*)
	MoS_2	48	5.86	0.12	0.862 (NaCl)	6.80	(*44*)

MXene	Pristine MXene	4.89	23.20	4.74	0.232 (KCl) 0.222 (NaCl)	100.00 104.50	(*45*)
	Thermal-treated MXene-180	4.89	13.89	2.86	3.4×10^{-3} (KCl) 6.7×10^{-3} (NaCl)	4.08×10^{3} 2.07×10^{3}	(*45*)
MOF	20 nm thick 2D Al-MOF	36	80.03	2.22	1.6×10^{-4} ($CoCl_2$)	5.00×10^{5}	This work
	50 nm thick 2D Al-MOF	36	51.35	1.43	1.3×10^{-4} ($CoCl_2$)	3.95×10^{5}	
	100 nm thick 2D Al-MOF	36	35.56	0.98	1.5×10^{-4} ($CoCl_2$)	2.37×10^{5}	
	150 nm thick 2D Al-MOF	36	20.71	0.58	1.3×10^{-4} ($CoCl_2$)	1.59×10^{5}	
	200 nm thick 2D Al-MOF	36	14.54	0.39	1.2×10^{-4} ($CoCl_2$)	1.21×10^{5}	
	100 nm thick 2D Al-MOF	24	2.44	0.10	1.5×10^{-4} (NaCl)	1.63×10^{4}	
	100 nm thick 2D Al-MOF	24	1.78	0.07	1.2×10^{-4} (KCl)	1.48×10^{4}	
	100 nm thick 2D Al-MOF	36	2.11	0.06	1.0×10^{-4}($MgCl_2$)	2.11×10^{4}	
	100 nm thick 2D Al-MOF	36	4.44	0.12	7.0×10^{-5} ($CaCl_2$)	6.35×10^{4}	
	100 nm thick 2D Al-MOF	48	24.44	0.51	8.0×10^{-5} ($AlCl_3$)	3.06×10^{5}	

* $\Delta\pi_{theo} = M \cdot R \cdot T$ is the van't Hoff equation used for the osmotic pressure's calculation in this study (*46*).

where M is the total molar mass of the draw solution (including cation and anion) (mol), R is the gas laws constant (0.0821) and T is the testing kelvin temperature (298.15 K). n/a: data not available.

Table S2. List of analyzed ions and their hydrated diameters. The following data were adapted from (*6*).

Ions and water	Hydrated diameter (Å)
K^+	6.62
Na^+	7.16
Mg^{2+}	8.56
Ca^{2+}	8.24
Co^{2+}	8.46
Al^{3+}	9.50
Cl^-	6.64
NO_3^-	6.80
SO_4^{2-}	10.00
H_2O	2.76

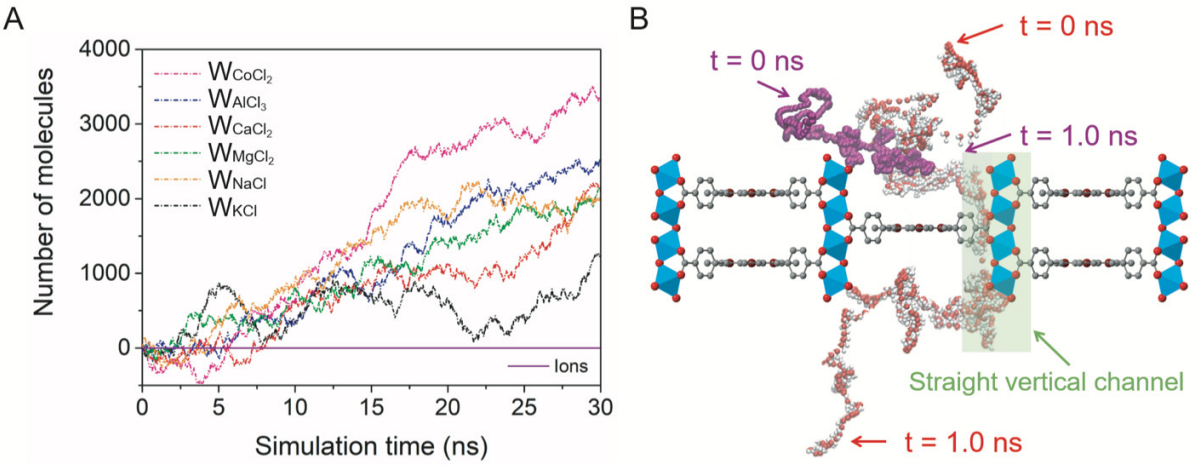

Fig. S31. Kinetic behaviour of water and ions transport across Al-MOF membranes. (**A**) Plots of H_2O and ions numbers flowing through one-layer Al-MOF nanosheet as a function of time from MD simulations. W_{ion} stands for the water molecules when a specific salt ion as the draw solution. (**B**) The trajectories of a Co^{2+} ion (displayed in purple) and a water molecular (displayed in red/white) across one-layer Al-MOF nanosheet in 1.0 ns.

Using equilibrium MD simulations, we computed the number of water and ions molecules permeated through the Al-MOF membrane. The draw solution used in the simulation is based on the experimental conditions (0.5 M salt aqueous solutions). Considering the redundant calculation consuming for this process, we hereby simplified the membrane structure to one-layer Al-MOF nanosheet throughout the MD simulation in this part. Fig. S31A shows the variation of the number of water molecules in the draw solution box with time. As the simulation progresses, the water molecules from the feed solution permeate through the membrane to the draw side due to the osmotic pressure. Consequently, the number of water molecules increases with time in the draw solution. However, all cations are effectively blocked by the pore apertures of Al-MOF, as no ions are found to flow through the Al-MOF nanosheet. The order of the water fluxes of the membrane using different salts is in good agreement with experimental results. Further illustration of collective ions and water motions across Al-MOF membrane were compared as shown in Fig. S31B. The water molecule follows a perpendicular pathway from the intrinsic pore of Al-MOF sheet during the permeation time of 1.0 ns. As compared to water molecule, Co^{2+} ion is stopped outside of the Al-MOF nanosheet at the end of passing process.

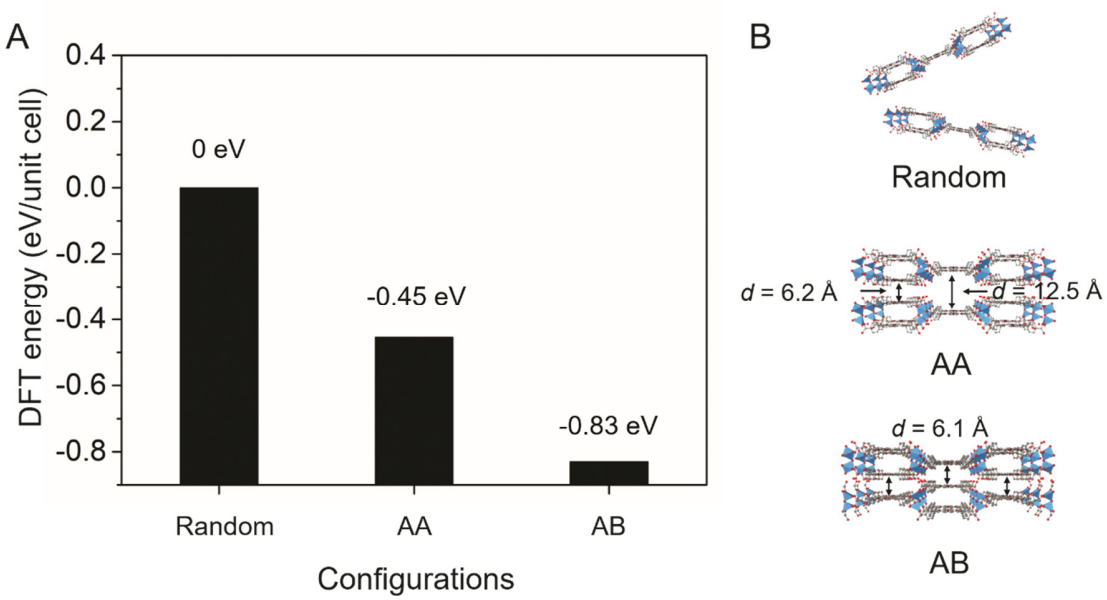

Fig. S32. The energy per unit cell at different configurations. (**A**) DFT energy/unit cell of three possible staking configurations is plotted as a function of the horizontal shift between two-layer Al-MOF sheets. (**B**) Schematic illustration of the three staking configurations (random, AA and AB stacking, respectively).

The energy per unit cell was obtained from DFT when shifting the top layer from different steps. We defaulted the first step as 0 eV/unit cell when it was in the random configuration (Fig. S32A,B). When the top layer is shifted along horizontal direction towards the "overlap" configuration, this shift arrangement is the well-known as AA stacking configuration (Fig. S32B). The barrier height for the "AA overlap" stacking is -0.45 eV/unit cell (Fig. S32A). By contrast, when the top layer is shifted in the opposite direction (AB stacking) (Fig. S32B), it has the lowest energy (-0.83 eV/unit cell) (Fig. S32A). Theoretically, both AA and AB stacking regimes possibly exist when Al-MOF nanosheets are assembled into laminar membranes. Nevertheless, DFT calculation reveals that AB stacking is more stable than AA stacking, as a result of a lower DFT energy. Furthermore, DFT calculation shows that the interspace of Al-MOF membrane formed *via* AB stacking is 6.1 Å, whereas there are two interlayer distances of 6.2 Å and 12.5 Å in AA stacking configuration.

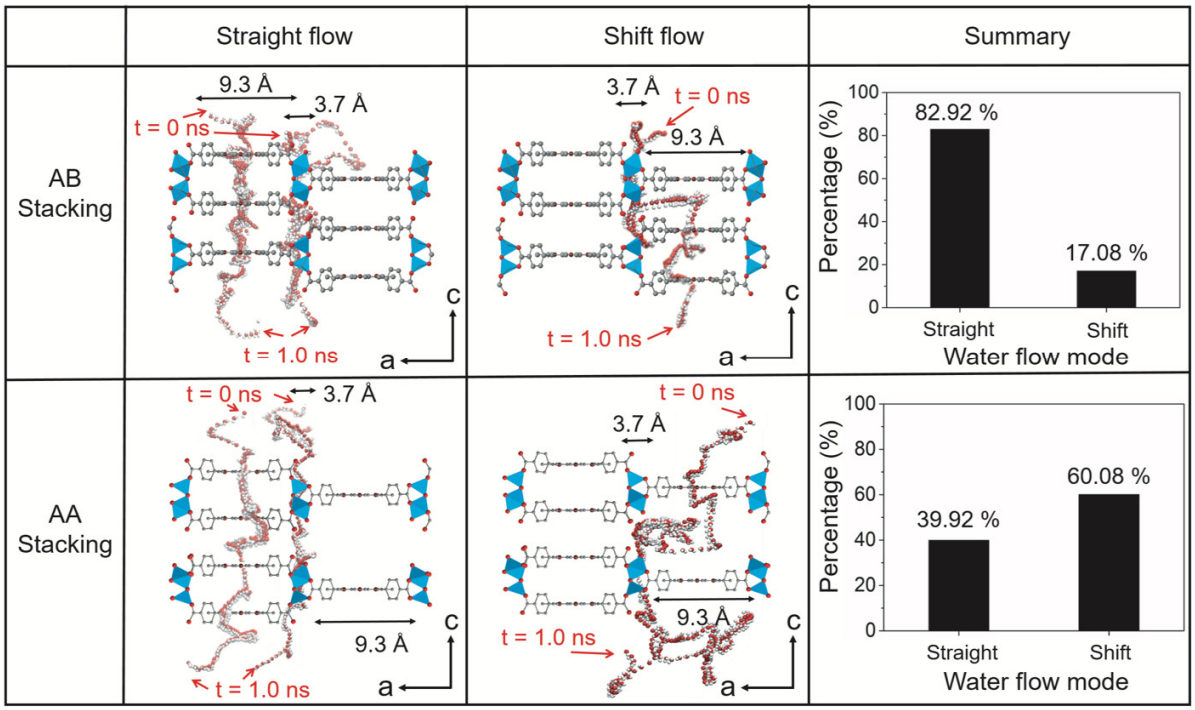

Fig. S33. Successive snapshots of the water molecule movements across Al-MOF membrane. Two-layer Al-MOF nanosheet under AB and AA stacking configurations were simulated. All snapshots were taken within 1.0 ns. The white and red spheres correspondingly denote the hydrogen and oxygen atoms, which make up the water molecule. Right figures summarize the possibility of water flow pathways accordingly under both stacking regimes. In total, 521 and 476 water molecules were counted in AB and AA stacking model, respectively.

In Fig. S33, water trajectories in the membranes constructed by two layers of Al-MOF nanosheets were investigated under AB and AA stacking configurations. Two distinct water flow pathways through the Al-MOF membrane were featured: straight and shift flows. Straight flow means that water molecule follows a straight pathway inside the layered Al-MOF membranes, in which water molecules merely pass through the vertically straight channels (see straight flow segment). By comparison, the lateral motion of water permeation across the membrane in some regions, particularly in the interlayer space, could take place. The shift flow refers to the water flow pathway where the lateral diffusion in adjacent pores is involved. It has been found that the possibility of water lateral shift flow in AA stacking (60.08 %) is greater than that in AB stacking (17.08 %) in the summarized histogram.

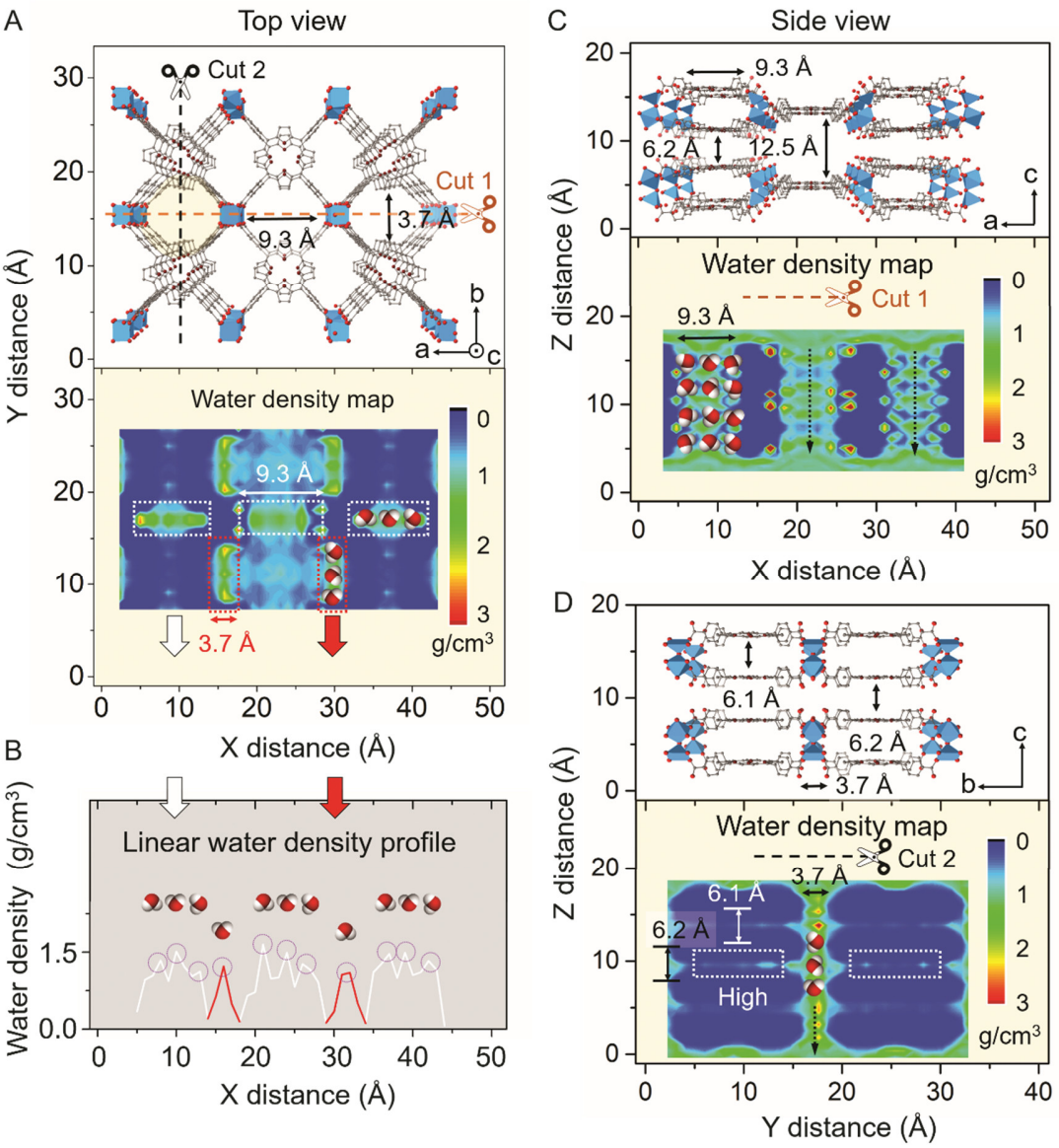

Fig. S34. Water transport behaviour through Al-MOF membranes. (**A**) Crystalline illustration of the Al-MOF membrane constructed with two-layer Al-MOF nanosheets under AA stacking sequence (viewed along the [010] direction). Dashed lines present two different incision positions for cross-sectional membrane geometries (marked with cut 1 and cut 2, respectively). Below figure is the corresponding water density map. The blue colour corresponds to no water existence and the red to the maximum water density. (**B**) Linear water density profile collected from the upper water density map. White lines represent the water density of pores (9.3 Å in X axis ×3.7 Å in Y axis), and red lines refer to that of pores (3.7 Å in X axis ×9.3 Å in Y axis), as illustrated in white and red dashed rectangles in the corresponding water density map in (A), respectively. (**C**) Side view of the membrane at cut 1 section viewed along the [001] direction, which gives two interlayer distances of 6.18 Å and 12.5 Å. Below figure is the corresponding water density map. (**D**) Side view of the membrane at cut 2 section viewed along the [100] direction. White dashed rectangles stand for the high water densities inside the interlayer space.

As a comparison, the Al-MOF membrane in AA stacking mode was investigated for the water dynamic transport. The assembling structure shows the identical entrance pore geometry to that in the AB stacking (Fig. S34A). However, side view of AA assembled membrane structure shows a different configuration, in which two different interlayer distances of 12.5 Å and 6.2 Å are formed (Fig. S34C). In terms of the water density map, a similar water distribution was observed to that in AB stacking situation, in which water diffusion is localized into the nanopores (Fig. S34A,B,C). Nevertheless, a small portion of water were found in the interlayer space, highlighted with the white dashed rectangles that display a high water density (Fig. S34D). This sort of diffusion process is slightly different from the phenomenon in the AB stacking, where the water molecules underwent a higher tortuosity than that in AB configuration. This should be attributed to the larger interlayer distance of 6.2 Å and 12.5 Å.

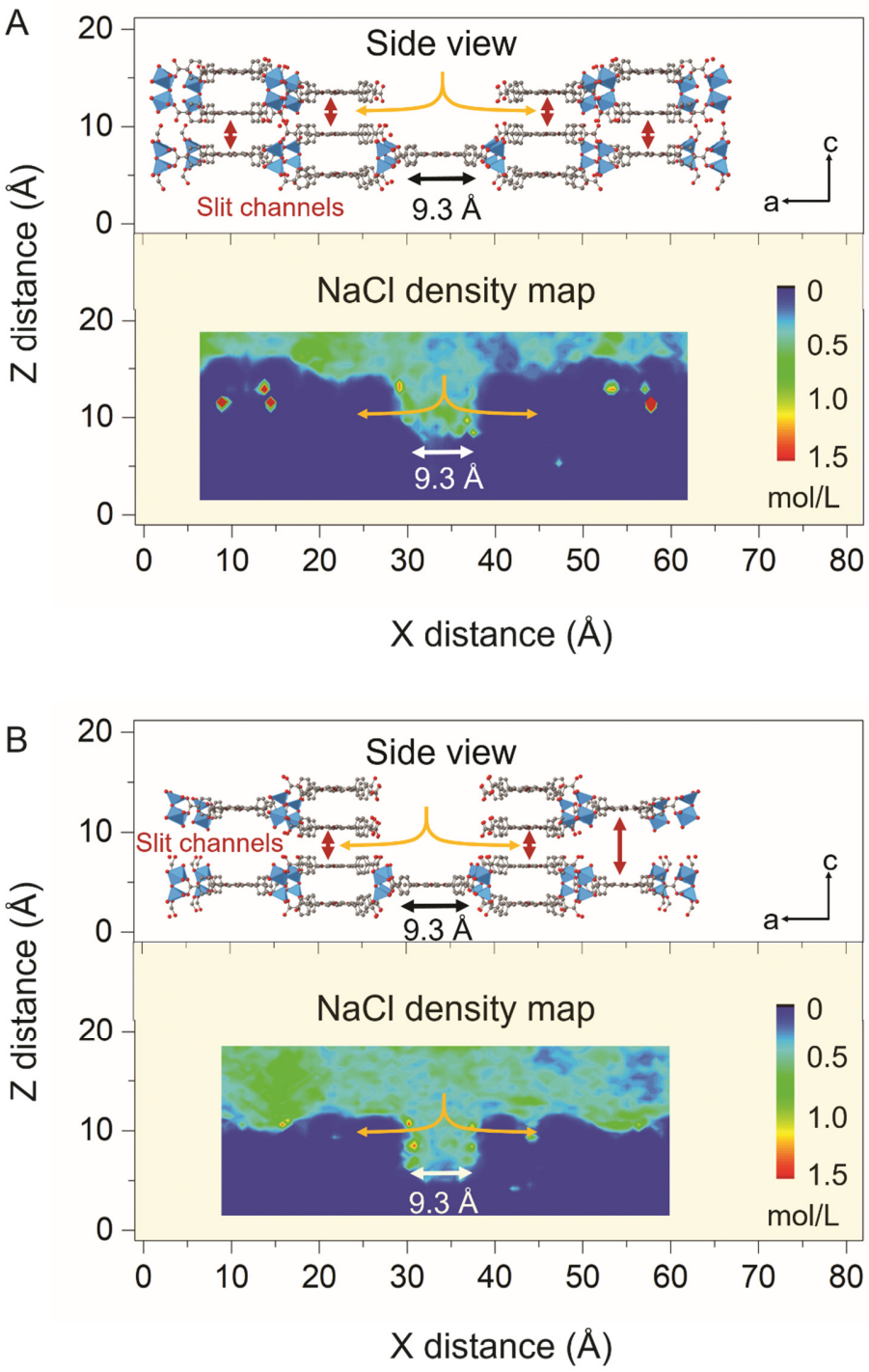

Fig. S35. NaCl diffusion process through Al-MOF membrane. Side view of the Al-MOF membrane under (A) AB stacking and (B) AA stacking sequences viewed along the [001] direction. Below figure is their corresponding NaCl concentration map after averaging from 2 ns filtration process.

With regard to the role of slit channels in the role of selectivity, the additional MD simulations for NaCl diffusion process through Al-MOF membrane were conducted. As shown in Fig. S35, we intentionally subtracted the middle part of Al-MOF nanosheet crystalline, in order to let the NaCl free flow through the first layer of Al-MOF nanosheet. Averaging from 2 ns filtration process, the corresponding below NaCl concentration map clearly reveals that the salt flow is basically limited in the slit channels of neighboring Al-MOF nanosheets.

REFERENCES AND NOTES

1. M. R. Chowdhury, J. Steffes, B. D. Huey, J. R. McCutcheon, 3D printed polyamide membranes for desalination. *Science* **361**, 682–686 (2018).

2. W. J. Koros, C. Zhang, Materials for next-generation molecularly selective synthetic membranes. *Nat. Mater.* **16**, 289–297 (2017).

3. J. R. Werber, C. O. Osuji, M. Elimelech, Materials for next-generation desalination and water purification membranes. *Nat. Rev. Mater.* **1**, 16018 (2016).

4. D. L. Gin, R. D. Noble, Designing the next generation of chemical separation membranes. *Science* **332**, 674–676 (2011).

5. H. B. Park, J. Kamcev, L. M. Robeson, M. Elimelech, B. D. Freeman, Maximizing the right stuff: The trade-off between membrane permeability and selectivity. *Science* **356**, eaab0530 (2017).

6. P. Wang, M. Wang, F. Liu, S. Y. Ding, X. Wang, G. Du, J. Liu, P. Apel, P. Kluth, C. Trautmann, Y. Wang, Ultrafast ion sieving using nanoporous polymeric membranes. *Nat. Commun.* **9**, 569 (2018).

7. M. Tsapatsis, Toward high-throughput zeolite membranes. *Science* **334**, 767–768 (2011).

8. R. H. Tunuguntla, R. Y. Henley, Y. C. Yao, T. A. Pham, M. Wanunu, A. Noy, Enhanced water permeability and tunable ion selectivity in subnanometer carbon nanotube porins. *Science* **357**, 792–796 (2017).

9. B. J. Hinds, N. Chopra, T. Rantell, R. Andrews, V. Gavalas, L. G. Bachas, Aligned multiwalled carbon nanotube membranes. *Science* **303**, 62–65 (2004).

10. I. Stassen, M. Styles, G. Grenci, H. Van Gorp, W. Vanderlinden, S. De Feyter, P. Falcaro, D. De Vos, P. Vereecken, R. Ameloot, Chemical vapour deposition of zeolitic imidazolate framework thin films. *Nat. Mater.* **15**, 304–310 (2016).

11. R. K. Joshi, P. Carbone, F. C. Wang, V. G. Kravets, Y. Su, I. V. Grigorieva, H. A. Wu, A. K. Geim, R. R. Nair, Precise and ultrafast molecular sieving through graphene oxide membranes. *Science* **343**, 752–754 (2014).

12. H. Liu, H. Wang, X. Zhang, Facile fabrication of freestanding ultrathin reduced graphene oxide membranes for water purification. *Adv. Mater.* **27**, 249–254 (2015).

13. Y. Kang, Y. Xia, H. Wang, X. Zhang, 2D laminar membranes for selective water and ion transport. *Adv. Funct. Mater.* **29**, 1902014 (2019).

14. Z. Zheng, R. Grünker, X. Feng, Synthetic two-dimensional materials: A new paradigm of membranes for ultimate separation. *Adv. Mater.* **28**, 6529–6545 (2016).

15. B. Mi, Materials science. Graphene oxide membranes for ionic and molecular sieving. *Science* **343**, 740–742 (2014).

16. J. Wang, P. Chen, B. Shi, W. Guo, M. Jaroniec, S.-Z. Qiao, A regularly channeled lamellar membrane for unparalleled water and organics permeation. *Angew. Chem. Int. Ed. Engl.* **57**, 6814–6818 (2018).

17. H. Furukawa, N. Ko, Y. B. Go, N. Aratani, S. B. Choi, E. Choi, A. O. Yazaydin, R. Q. Snurr, M. O'Keeffe, J. Kim, O. M. Yaghi, Ultrahigh porosity in metal-organic frameworks. *Science* **329**, 424–428 (2010).

18. S. Qiu, M. Xue, G. Zhu, Metal-organic framework membranes: From synthesis to separation application. *Chem. Soc. Rev.* **43**, 6116–6140 (2014).

19. X. Li, Y. Liu, J. Wang, J. Gascon, J. Li, B. Van der Bruggen, Metal–organic frameworks based membranes for liquid separation. *Chem. Soc. Rev.* **46**, 7124–7144 (2017).

20. Y. Peng, Y. Li, Y. Ban, H. Jin, W. Jiao, X. Liu, W. Yang, Membranes. Metal-organic framework nanosheets as building blocks for molecular sieving membranes. *Science* **346**, 1356–1359 (2014).

21. M. S. Denny Jr., J. C. Moreton, L. Benz, S. M. Cohen, Metal–organic frameworks for membrane-based separations. *Nat. Rev. Mater.* **1**, 16078 (2016).

22. A. J. Howarth, Y. Liu, P. Li, Z. Li, T. C. Wang, J. T. Hupp, O. K. Farha, Chemical, thermal and mechanical stabilities of metal–organic frameworks. *Nat. Rev. Mater.* **1**, 15018 (2016).

23. A. Fateeva, P. A. Chater, C. P. Ireland, A. A. Tahir, Y. Z. Khimyak, P. V. Wiper, J. R. Darwent, M. J. Rosseinsky, A water-stable porphyrin-based metal–organic framework active for visible-light photocatalysis. *Angew. Chem. Int. Ed.* **51**, 7440–7444 (2012).

24. Y. Jiang, L. Cao, X. Hu, Z. Ren, C. Zhang, C. Wang, Simulating powder X-ray diffraction patterns of two-dimensional materials. *Inorg. Chem.* **57**, 15123–15132 (2018).

25. S. Motoyama, R. Makiura, O. Sakata, H. Kitagawa, Highly crystalline nanofilm by layering of porphyrin metal−organic framework sheets. *J. Am. Chem. Soc.* **133**, 5640–5643 (2011).

26. R. Makiura, S. Motoyama, Y. Umemura, H. Yamanaka, O. Sakata, H. Kitagawa, Surface nano-architecture of a metal–organic framework. *Nat. Mater.* **9**, 565–571 (2010).

27. M. P. Jian, H. Y. Liu, T. Williams, J. S. Ma, H. T. Wang, X. W. Zhang, Temperature-induced oriented growth of large area, few-layer 2D metal-organic framework nanosheets. *Chem. Commun.* **53**, 13161–13164 (2017).

28. M. Rastgar, A. Bozorg, A. Shakeri, Novel dimensionally controlled nanopore forming template in forward osmosis membranes. *Environ. Sci. Technol.* **52**, 2704–2716 (2018).

29. W. A. Phillip, J. S. Yong, M. Elimelech, Reverse draw solute permeation in forward osmosis: Modeling and experiments. *Environ. Sci. Technol.* **44**, 5170–5176 (2010).

30. Y. Wang, R. Ou, H. Wang, T. Xu, Graphene oxide modified graphitic carbon nitride as a modifier for thin film composite forward osmosis membrane. *J. Membr. Sci.* **475**, 281–289 (2015).

31. N.-N. Bui, J. R. McCutcheon, Nanoparticle-embedded nanofibers in highly permselective thin-film nanocomposite membranes for forward osmosis. *J. Membr. Sci.* **518**, 338–346 (2016).

32. J. Tóth, *Adsorption: Theory, Modeling, and Analysis* (Marcel Dekker Inc., 2002), vol. 107, 878 pp.

33. J. Gasteiger, M. Marsili, Iterative partial equalization of orbital electronegativity—A rapid access to atomic charges. *Tetrahedron* **36**, 3219–3228 (1980).

34. P. Li, L. F. Song, K. M. Merz Jr., Parameterization of highly charged metal ions using the 12-6-4 LJ-type nonbonded model in explicit water. *J. Phys. Chem. B* **119**, 883–895 (2014).

35. J. R. Werber, A. Deshmukh, M. Elimelech, The critical need for increased selectivity, not increased water permeability, for desalination membranes. *Environ. Sci. Technol. Lett.* **3**, 112–120 (2016).

36. X. Zou, G. Zhu, I. J. Hewitt, F. Sun, S. Qiu, Synthesis of a metal-organic framework film by direct conversion technique for VOCs sensing. *Dalton Trans.* 3009–3013 (2009).

37. A. Fidalgo-Marijuan, G. Barandika, B. Bazán, M. K. Urtiaga, E. S. Larrea, M. Iglesias, L. Lezama, M. I. Arriortua, Heterogeneous catalytic properties of unprecedented μ-*O*-[FeTCPP]$_2$ dimers (H_2TCPP = *meso*-tetra(4-carboxyphenyl)porphyrin): An unusual superhyperfine EPR structure. *Dalton Trans.* **44**, 213–222 (2015).

38. H.-Y. Zeng, J.-Z. Du, S. Xu, M.-C. Liao, X.-J. Liu, H.-Z. Duan, C.-R. Chen, Influences of a glycerin co-solvent on the compatibility of MgAl hydrotalcites with a polypropylene matrix. *RSC Adv.* **5**, 64814–64820 (2015).

39. L. G. Joyner, E. P. Barrett, R. Skold, The determination of pore volume and area distributions in porous substances. II. Comparison between nitrogen isotherm and mercury porosimeter methods. *J. Am. Chem. Soc.* **73**, 3155–3158 (1951).

40. W. L. Xu, C. Fang, F. Zhou, Z. Song, Q. Liu, R. Qiao, M. Yu, Self-assembly: A facile way of forming ultrathin, high-performance graphene oxide membranes for water purification. *Nano Lett.* **17**, 2928–2933 (2017).

41. L. Chen, G. Shi, J. Shen, B. Peng, B. Zhang, Y. Wang, F. Bian, J. Wang, D. Li, Z. Qian, G. Xu, G. Liu, J. Zeng, L. Zhang, Y. Yang, G. Zhou, M. Wu, W. Jin, J. Li, H. Fang, Ion sieving in graphene oxide membranes via cationic control of interlayer spacing. *Nature* **550**, 380–383 (2017).

42. J. Abraham, K. S. Vasu, C. D. Williams, K. Gopinadhan, Y. Su, C. T. Cherian, J. Dix, E. Prestat, S. J. Haigh, I. V. Grigorieva, P. Carbone, A. K. Geim, R. R. Nair, Tunable sieving of ions using graphene oxide membranes. *Nat. Nanotechnol.* **12**, 546–550 (2017).

43. W. Hirunpinyopas, E. Prestat, S. D. Worrall, S. J. Haigh, R. A. W. Dryfe, M. A. Bissett, Desalination and nanofiltration through functionalized laminar MoS_2 membranes. *ACS Nano* **11**, 11082–11090 (2017).

44. M. Deng, K. Kwac, M. Li, Y. Jung, H. G. Park, Stability, molecular sieving, and ion diffusion selectivity of a lamellar membrane from two-dimensional molybdenum disulfide. *Nano Lett.* **17**, 2342–2348 (2017).

45. Z. Lu, Y. Wei, J. Deng, L. Ding, Z. K. Li, H. Wang, Self-crosslinked MXene ($Ti_3C_2T_x$) membranes with good antiswelling property for monovalent metal ion exclusion. *ACS Nano* **13**, 10535–10544 (2019).

46. R. A. Robinson, R. H. Stokes, *Electrolyte Solutions* (Dover Publications, ed. 2, 2002).